Final Report

for

Development of an Improved Radiation Resistant Solar Cell
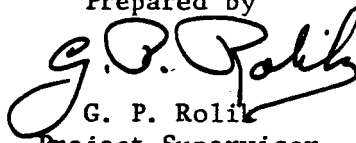
27 September 1963 - 27 December 1964

Contract No.: NAS5-3560

Prepared by

Electro-Optical Systems, Inc.
Pasadena, California

for

Goddard Space Flight Center
Greenbelt, Maryland

RQT 26384

Final Report

for

Development of an Improved Radiation Resistant Solar Cell

27 September 1963 — 27 December 1964

Contract No.:   NAS5-3560

Prepared by

G. P. Rolik
Project Supervisor

Approved by

S. Kaye, Manager
Semiconductor Department

Approved by

M. B. Prince, Manager
Aerospace Electronics Division

Electro-Optical Systems, Inc.
Pasadena, California
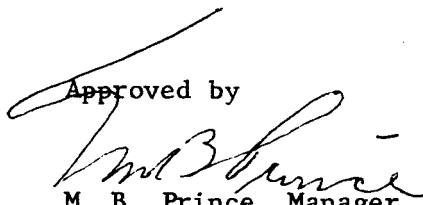
for

Goddard Space Flight Center
Greenbelt, Maryland

ABSTRACT

19687

The results of a program to develop an improved radiation resist-
ant solar cell by the incorporation of an electric field are described.
Included are the results of a theoretical computer evaluation, drift
field fabrication experiments, and radiation damage data.

A significant correlation was observed between the theoretical
considerations and experimental results, which showed that the optimum
drift field thickness lies between 50 and 100 microns. Recommendations
for future work are included in the final report.

AUTHOR-P

CONTENTS (Contd)

FIGURES

FIGURES (Contd)

TABLES

1. INTRODUCTION

The objective of this contract was the development of an improved radiation resistant, drift field solar cell which would be capable of good performance after prolonged exposure to space radiation environments. It was decided in consultation with the technical monitor for this contract at Goddard Space Flight Center to have as a design goal, an n-on-p type drift field cell with the following characteristics after 5 years in an orbit equivalent to that of OGO or OSO:

Cover glass thickness	0.060 inch
1 Mev electron, equivalent flux	2×10^{15} particles/cm^2
Average diffusion length of minority carriers	25×10^{-4} cm
Average lifetime of minority carriers	3×10^{-7} seconds
Drift field voltage	0.3 to 0.36 volt
Drift field region thickness	40 to 50×10^{-4} cm
Average field strength	75 to 90 volts/cm
Ratio of short circuit current after 5 years to initial short circuit current	Sunlight 0.9 Tungsten 0.85
Comparative ratio of short circuit current after 5 years to initial short circuit current of n-on-p zero drift field cell	0.78

It was initially proposed to investigate fabrication procedures of forming drift field structures using three different approaches:

1. Aluminum alloy diffused approach

2. Front epitaxial approach

3. Reverse epitaxial approach

The program was essentially divided into three phases. Work during Phase I of the contract included fabrication of prototype samples, using all three approaches. The aluminum alloy-diffused method was

found to possess several inherent difficulties and the solutions were deemed to be beyond the scope of the contract, although several cells employing this technique were submitted. The front epitaxial approach, which primarily evidenced some promise, later proved to be incompatible with the epitaxial system and procedures being used. As a result the reverse epitaxial approach was undertaken and cells were fabricated that showed good I-V characteristics.

Work performed during Phase II of the contract included:

1. Fabrication of larger quantities of drift field cells using the reverse epitaxial approach

2. Measurement of the I-V characteristics in sunlight and tungsten of all such cells

3. Measurement of the spectral response of representative cells from each pilot production lot

Phase III consisted primarily of submission of sample cells to the contract monitor for particle irradiation and analysis of the radiation damage data as made available by the contract monitor.

The scope and purpose of this report is an exhaustive summary of the work performed during all three phases of the contract. Included are the results of a computer solution of the solar cell continuity equation, performed with the cooperation of the contract monitor.

2. THEORETICAL CONSIDERATIONS

2.1 Method of Solution of Solar Cell Continuity Equation

To gain insight into the problem of the optimum drift field thickness required to render solar cells more radiation resistant for use in near-earth orbit missions, it was decided to attempt a solution of the solar cell continuity equation. This equation, expressed as:

$$D \frac{d^2 n}{dx^2} + \left[\frac{dD}{dx} + \mu E \right] \frac{dn}{dx} + \left[E \frac{d\mu}{dx} + \mu \frac{dE}{dx} - \frac{1}{\tau} \right] n =$$

$$- \int_0^{\lambda_G} N(\lambda)\, \alpha(\lambda) e^{-\alpha(\lambda)x}\, d\lambda \qquad (1)$$

where

n = excess carrier concentration

μ = mobility of carriers in base region

E = drift field

D = diffusion constant of carriers

x = distance from p-n junction

τ = minority lifetime of carriers

N = number of photons

α = absorption coefficient of the material

λ = wavelength

λ_G = wavelength corresponding to the energy gap of the material

was first considered by Kleinman (Ref. 1). A partial computer evaluation was effected by Cheslow and Kaye (Ref. 2), who assumed E, μ, and D to be independent of x, gaining a fair preliminary insight into drift field behavior. Wolf (Ref. 3) has shown theoretically that multilayer drift field cells would be more radiation resistant than conventional

cells by obtaining a quasi-analytical solution to the equation, assuming E, μ, and D to be constant in x and simplifying the forcing integral to be dependent on x alone.

Because of the complicated nature of the forcing term containing x under the integral, a purely analytical solution to Eq. 1 is nonexistent. As a result, it was decided to abandon the use of an analytical approach, and substitute instead the technique of numerical solution by successive approximation using the computer facility at Goddard Space Flight Center.

Equation 1 was modified to yield

$$\frac{kT}{q}(C_1 + Px)\frac{d^2n}{dx^2} + \left[P\left(\frac{kT}{q}\right) + (C_1 + Px)\left(\frac{0.6}{w} - \frac{0.6x}{w^2}\right)\right]\frac{dn}{dx} +$$

$$\left[P\left(\frac{0.6}{w} - \frac{0.6x}{w^2}\right) - \frac{0.6}{w^2}(C_1 + Px) - \frac{1}{\tau}\right]n =$$

$$-\sum_{j=1}^{10} N(\lambda)_j \, \alpha(\lambda)_j \, e^{-\alpha(\lambda)_j x}(0.33R_j) \qquad (2)$$

upon substitution of the following identities, assuming a linear dependence on x of μ, E, and τ in the p-type base region:

$\mu = C_1 + Px$, mobility of electrons in $cm^2 \, sec^{-1} \, volt^{-1}$

$\frac{d\mu}{dx} = P$ in $cm \, sec^{-1} \, volt^{-1}$

$D = \mu\left(\frac{kT}{q}\right) = (C_1 + Px)\frac{kT}{q}$, diffusion constant of electrons
by Einstein relation in $cm^2 \, sec^{-1}$

$\frac{dD}{dx} = P\left(\frac{kT}{q}\right)$ in $cm \, sec^{-1}$

$E = \frac{0.6}{w} - \frac{0.6x}{w^2}$ = field in volts cm^{-1} where w is the boundary
between the active (drift-field) and passive
regions

$\frac{dE}{dx} = \frac{0.6}{w^2}$ in volts cm^{-2}

The validity of these linear relationships can be shown upon consideration of the present technique of forming drift field structures by diffusion. The back of the active region has a high concentration of impurities, approaching 10^{21} cm^{-3}, with an erfc distribution decrease toward the front nearer the p-n junction. The essential shape of the erfc curve presupposes a zero value field at the back and increasing toward the front. The electron mobility essentially low in the low resistivity material at the back, approximately 40 cm^2 volt^{-1} sec^{-1}, also increases, to a value of approximately 1400 cm^2 volt^{-1} sec^{-1} in the 25 ohm-cm material at the front (Refs. 2 and 4). Although neither of these quantities is a linear function, assuming them to be linear in x in the active portion of the cell is a valid first approximation.

The two boundary conditions necessary for solution of Eq. 1 can be determined by:

1. Considering the depletion region at the junction to be an infinite sink for excess carriers, so that

$$n(x_j) = 0 \tag{3}$$

2. Considering the equation governing the passive layer toward the back of the cell as:

$$\frac{d^2 n}{dx^2} - \frac{n}{D\tau} = 0 \tag{4}$$

which assumes μ to be constant, E to be zero, and the forcing term

$$-\int_0^{\lambda_G} N(\lambda)\alpha(\lambda)e^{-\alpha(\lambda)x}\, d\lambda$$

to be negligible. The solution to Eq. 4 is:

$$n(x) = Ae^{-x/L} + Be^{x/L} \quad \text{where } L^2 = D\tau \tag{5}$$

Since n $(\infty) = 0$, B = 0. Solving for A and taking the first derivative yields:

$$\frac{dn(w)}{dx} = - \frac{n(w)}{L} = - \frac{n(w)}{\sqrt{\tau(C_1 + Pw)\frac{kT}{q}}} \qquad (6)$$

Since $\frac{dn(w)}{dx}$ for Eq. 1 is identical to $\frac{dn(w)}{dx}$ for Eq. 4, by definition for preservation of continuity, the secondary boundary condition is established.

The constants A and B in any resulting solution of Eq. 1 can be determined from these conditions. The general solution to Eq. 1 can be expressed in the form:

$$n_1(x) = A_1 f_1(x) + B_1 f_2(x) + f_3(x) \qquad (7)$$

and the solution for Eq. 4 as

$$n_2(x) = A_2 f_4(x) \qquad (8)$$

Since

$$n(x_j) = 0,$$

$$n_1(x_j) = A_1 f_1(x_j) + B_1 f_2(x_j) + f_3(x_j) = 0 \qquad (9)$$

By substituting Eqs. 7 and 8 into the two conditions for preservation of continuity of x = w, namely:

$$n_1(w) = n_2(w) \qquad (10a)$$

and

$$\frac{dn_1(w)}{dx} = \frac{dn_2(w)}{dx} \qquad (10b)$$

we obtain:

$$A_1 f_1(w) + B_1 f_2(w) + f_3(w) = A_2 f_4(w) \qquad (11a)$$

and

$$A_1 f_1'(w) + B_1 f_2'(w) + f_3'(w) = A_2 f_4'(w) \qquad (11b)$$

A_2 can be solved out in Eqs. 11a and 11b by equating and by rearrangement of terms, this yields

$$A_1 \left[\frac{f_1'(w)}{f_4'(w)} - \frac{f_1(w)}{f_4(w)}\right]_1 + B_1 \left[\frac{f_2'(w)}{f_4'(w)} - \frac{f_2(w)}{f_4(w)}\right]_2 = \left[\frac{f_3(w)}{f_4(w)} - \frac{f_3'(w)}{f_4'(w)}\right]_3 \qquad (12a)$$

this equation plus a rearranged form of Eq. 9:

$$A_1 f_1(x_j) + B_1 f_2(x_j) = -f_3(x_j) \qquad (12b)$$

being two linear equations of two unknowns which can be solved by determinants yielding:

$$A_1 = \frac{\begin{vmatrix} [\quad]_3 & [\quad]_2 \\ -f_3(x_j) & f_2(x_j) \end{vmatrix}}{\begin{vmatrix} [\quad]_1 & [\quad]_2 \\ f_1(x_j) & f_2(x_j) \end{vmatrix}} \quad \text{and} \quad B_1 = \frac{\begin{vmatrix} [\quad]_1 & [\quad]_3 \\ f_1(x_j) & -f_3(x_j) \end{vmatrix}}{\begin{vmatrix} [\quad]_1 & [\quad]_2 \\ f_1(x_j) & f_2(x_j) \end{vmatrix}} \qquad (13)$$

the numbered brackets corresponding to the numbered brackets in Eq. 12a.

For digital solution by computer, the following values were utilized:

1. For the gaussian quadrature evaluation of the forcing integral:

	λ(in μ)	0.33R (in μ)	α(in cm^{-1})	N (in cm^{-2} μ^{-1} sec^{-1})
1.	0.429	2.20×10^{-2}	3.7×10^{4}	3.9×10^{17}
2.	0.465	4.92×10^{-2}	2.0×10^{4}	5.0×10^{17}
3.	0.526	7.23×10^{-2}	9.0×10^{3}	5.2×10^{17}
4.	0.607	8.88×10^{-2}	4.3×10^{3}	5.4×10^{17}
5.	0.701	9.77×10^{-2}	2.2×10^{3}	5.0×10^{17}
6.	0.799	9.77×10^{-2}	1.03×10^{3}	4.5×10^{17}
7.	0.893	8.88×10^{-2}	4.5×10^{2}	4.1×10^{17}
8.	0.974	7.23×10^{-2}	1.56×10^{2}	3.7×10^{17}
9.	1.035	4.92×10^{-2}	42.0	3.5×10^{17}
10.	1.071	2.20×10^{-2}	17.0	3.5×10^{17}

2. For the constants at 300°K:

$\frac{kT}{q} = 0.026$, $\frac{q}{kT} = 38.5$, $C_1 = 1500$ cm^2 sec^{-1} volt^{-1},

3. For the variables:

25μ wide drift field

$w = 2.5 \times 10^{-3}$ cm

$P = -5.8 \times 10^{5}$ cm sec^{-1}

$\left.\begin{array}{l} \tau = 10^{-5} \text{ secs} \\ \quad = 3 \times 10^{-6} \text{ secs} \\ \quad = 10^{-6} \text{ secs} \\ \quad = 3 \times 10^{-7} \text{ secs} \end{array}\right\}$ at $x = x_j = 5 \times 10^{-5}$ cm

$\left.\begin{array}{l} \tau = 10^{-6} \text{ secs} \\ \quad = 3 \times 10^{-7} \text{ secs} \\ \quad = 10^{-7} \text{ secs} \\ \quad = 3 \times 10^{-8} \text{ secs} \end{array}\right\}$ at $x = w = 2.5 \times 10^{-3}$ cm

50μ wide drift field

$w = 5 \times 10^{-3}$ cm

$P = -2.9 \times 10^5$ cm sec^{-1}

$\tau = 10^{-5}$ secs
$= 3 \times 10^{-6}$ secs
$= 10^{-6}$ secs
$= 3 \times 10^{-7}$ secs
$\Big\}$ at $x = x_j = 5 \times 10^{-5}$ cm

$\tau = 10^{-6}$ secs
$= 3 \times 10^{-7}$ secs
$= 10^{-7}$ secs
$= 3 \times 10^{-8}$ secs
$\Big\}$ at $x = w = 5 \times 10^{-3}$ cm

60μ wide drift field

$w = 6 \times 10^{-3}$ cm

$P = -2.4 \times 10^5$ cm sec^{-1}

$\tau = 10^{-5}$ secs
$= 3 \times 10^{-6}$ secs
$= 10^{-6}$ secs
$= 3 \times 10^{-7}$ secs
$\Big\}$ at $x = x_j = 5 \times 10^{-5}$ cm

$\tau = 10^{-6}$ secs
$= 3 \times 10^{-7}$ secs
$= 10^{-7}$ secs
$= 3 \times 10^{-8}$ secs
$\Big\}$ at $x = w = 6 \times 10^{-3}$ cm

80μ wide drift field

$w = 8 \times 10^{-3}$ cm

$P = -1.8 \times 10^5$ cm sec^{-1}

$\tau = 10^{-5}$ secs
$= 3 \times 10^{-6}$ secs
$= 10^{-6}$ secs
$= 3 \times 10^{-7}$ secs
$\Big\}$ at $x = x_j = 5 \times 10^{-5}$ cm

$$\left. \begin{array}{l} \tau = 10^{-6} \text{ secs} \\ = 3 \times 10^{-7} \text{ secs} \\ = 10^{-7} \text{ secs} \\ = 3 \times 10^{-8} \text{ secs} \end{array} \right\} \quad \text{at } x = w = 8 \times 10^{-3} \text{ cm}$$

100μ wide drift field

$w = 10^{-2}$ cm

$P = -1.45 \times 10^5$ cm sec^{-1}

$$\left. \begin{array}{l} \tau = 10^{-5} \text{ secs} \\ = 3 \times 10^{-6} \text{ secs} \\ = 10^{-6} \text{ secs} \\ = 3 \times 10^{-7} \text{ secs} \end{array} \right\} \quad \text{at } x = x_j = 5 \times 10^{-5} \text{ cm}$$

$$\left. \begin{array}{l} \tau = 10^{-6} \text{ secs} \\ = 3 \times 10^{-7} \text{ secs} \\ = 10^{-7} \text{ secs} \\ = 3 \times 10^{-8} \text{ secs} \end{array} \right\} \quad \text{at } x = w = 10^{-2} \text{ cm}$$

125μ wide drift field

$w = 1.25 \times 10^{-2}$

$P = -1.16 \times 10^5$ cm sec^{-1}

$$\left. \begin{array}{l} \tau = 10^{-5} \text{ secs} \\ = 3 \times 10^{-6} \text{ secs} \\ = 10^{-6} \text{ secs} \\ = 3 \times 10^{-7} \text{ secs} \end{array} \right\} \quad \text{at } x = x_j = 5 \times 10^{-5} \text{ cm}$$

$$\left. \begin{array}{l} \tau = 10^{-6} \text{ secs} \\ = 3 \times 10^{-7} \text{ secs} \\ = 10^{-7} \text{ secs} \\ = 3 \times 10^{-8} \text{ secs} \end{array} \right\} \quad \text{at } x = w = 1.25 \times 10^{-2} \text{ cm}$$

150μ wide drift field

$w = 1.5 \times 10^{-2}$ cm

$P = -9.7 \times 10^{4}$ cm sec^{-1}

$\left.\begin{array}{l} \tau = 10^{-5} \text{ secs} \\ = 3 \times 10^{-6} \text{ secs} \\ = 10^{-6} \text{ secs} \\ = 3 \times 10^{-7} \text{ secs} \end{array}\right\}$ at $x = x_j = 5 \times 10^{-5}$ cm

$\left.\begin{array}{l} \tau = 10^{-6} \text{ secs} \\ = 3 \times 10^{-7} \text{ secs} \\ = 10^{-7} \text{ secs} \\ = 3 \times 10^{-8} \text{ secs} \end{array}\right\}$ at $x = w = 1.5 \times 10^{-2}$ cm

200μ wide drift field

$w = 2 \times 10^{-2}$ cm

$P = -7.25 \times 10^{4}$ cm sec^{-1}

$\left.\begin{array}{l} \tau = 10^{-5} \text{ secs} \\ = 3 \times 10^{-6} \text{ secs} \\ = 10^{-6} \text{ secs} \\ = 3 \times 10^{-7} \text{ secs} \end{array}\right\}$ at $x = x_j = 5 \times 10^{-5}$ cm

$\left.\begin{array}{l} \tau = 10^{-6} \text{ secs} \\ = 3 \times 10^{-7} \text{ secs} \\ = 10^{-7} \text{ secs} \\ = 3 \times 10^{-8} \text{ secs} \end{array}\right\}$ at $x = w = 2 \times 10^{-2}$ cm

2.2   Results of Computer Solution

The computer was programmed to yield digital solutions to Eq. 2 using the data enumerated above, and values of excess carrier density n were obtained for various distances x between x_j and $x = w$. Also obtained was the value of the total flow of generated carriers $D \frac{\delta n}{\delta x}$ at x_j for the four combinations of life times τ, at each of the eight field thicknesses. The collection efficiency η_B of the base drift field region was calculated from the relation:

$$\eta_B = \frac{D \frac{\delta n}{\delta x}}{\int_0^\infty N(\lambda) d\lambda} \tag{14}$$

the integral being the total number of incident photons at air mass zero which, according to Kleinman, is 3.3×10^{17} photons cm^{-2} (Ref. 1).

Figure 1 shows the plot of the calculations of base collection efficiency versus drift field thickness at various residual minority carrier lifetimes. It is apparent that for low residual lifetimes, in the vicinity of 10^{-7} to 10^{-8} secs, an optimum field thickness exists between 50 to 75 microns. Although at thin field widths, $<50\mu$, the flow of carriers appears to be independent of residual lifetime, the collection efficiency contributions from the base field region becomes quite low.

The salient feature of the data is the fact that, as residual lifetime decreases, the optimum field thickness decreases, as indicated by the slant line in Fig. 1 connecting the maxima of the functions. It would thus seem feasible to construct drift field cells optimum for each specific mission dependent on the total radiation flux expected. However, it is felt at this time that for residual lifetimes of 10^{-7} secs corresponding to a total flux of 10^{16} one Mev electrons, drift field thicknesses of 50 to 100μ would seem to produce optimum behavior.

In Fig. 2 is plotted the total collection efficiency versus residual lifetime of a near optimum drift field cell and a standard field free cell. It is apparent that, at higher minority carrier lifetimes, the field free cell has a higher total collection efficiency providing an initially higher short circuit current. However, at low residual lifetimes, approaching $<10^{-7}$ secs, the drift field cell has a collection efficiency of 20 percent higher.

This data, at least on a theoretical basis, would indicate higher collection efficiency and consequent short-circuit current retention by drift field solar cells after radiation fluxes of 10^{16} one Mev electrons giving fair insight into the short circuit degradation problem.
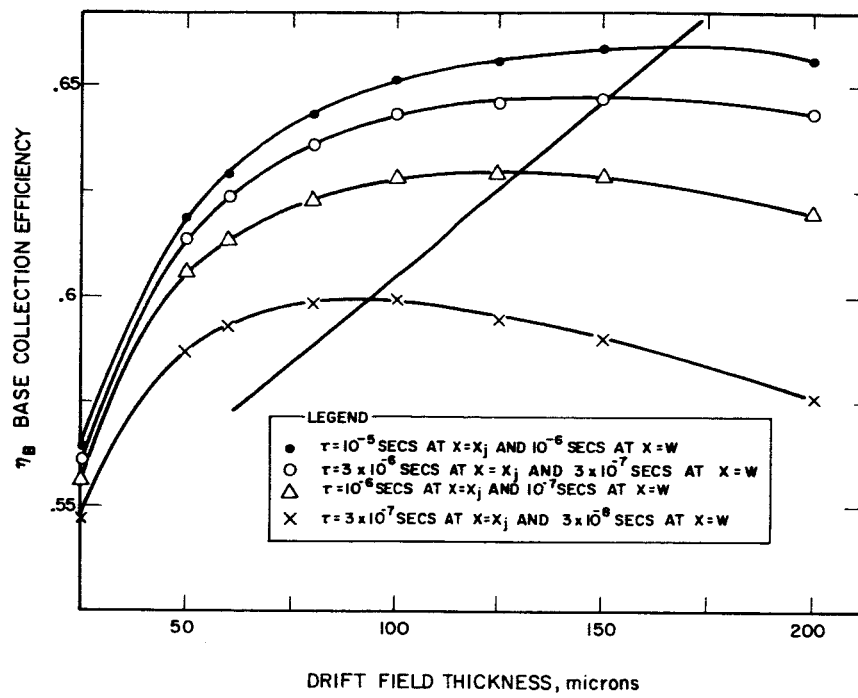
FIG. 1   RESULTS OF COMPUTER PROGRAM
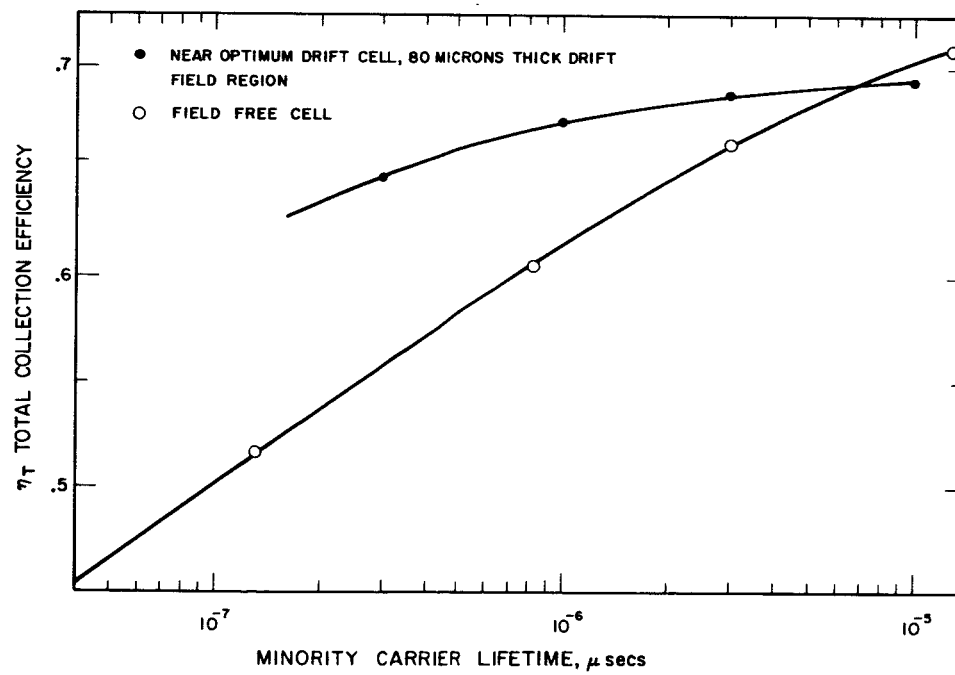
FIG. 2   COLLECTION EFFICIENCY OF NEAR OPTIMUM DRIFT
CELL VERSUS FIELD FREE CELL

2.3 Open Circuit Voltage Degradation

The explanation of degradation of open circuit voltage is, however, not as clear as that of short circuit current degradation. Since the open circuit voltage is dependent on many factors, including the light generated current I_L, saturation current I_o, the diode equation A factor, and the band structure in the vicinity of the junction, the picture is extremely complex at present.

Upon solution of the diode equation

$$I = I_o \left[\exp \left(\frac{qV}{AKT} \right) - 1 \right] + I_L \tag{15}$$

for V in terms of I, assuming I_o to be much smaller than I_L, the following relation ensues:

$$V_{OC} = \frac{AKT}{q} \ln \left| \frac{I_L}{I_o} \right| \tag{16}$$

Fair values of I_o may be gained by a plot of $\log |I - I_{sc}|$ versus voltage from solar cell I-V characteristic curves. Upon extrapolation to V = 0 of the slope of the plot at the I_L dominated portion of the I-V characteristic well above the "knee" of the curve, an empirical value of I_o can be obtained.

The validity of this can be shown by considering Eq. 15 in a rearranged form:

$$\ln(I - I_L) = \frac{qV}{AKT} + \ln I_o \tag{17}$$

again assuming $I_o \ll I_L$. Since the factor A changes with voltage, the plot of $\ln(I - I_L)$ will approach zero as V approaches zero. However if an extrapolation is made to V = 0 from that portion of the plot where $1 < A < 2$, the value of I_o obtained is that value near the maximum power point of the I-V characteristic curve. The dependence of I_o on the value of A can be shown upon differentiation of Eq. 15:

$$\frac{\delta I}{\delta V} = \frac{I_o q}{AKT} \exp(qV/AKT) \qquad (18)$$

$$I_o = \frac{AKT\ (\delta I/\delta V)}{q} \exp -\left(\frac{qV}{AKT}\right) \qquad (19)$$

Because of these relations, it would be well to consider the nature of the saturation current in a diode and its possible increase after particle irradiation. Jonscher has shown the dependence of saturation current generation on minority carrier lifetime in the space charge region as (Ref. 5):

$$J_g = q\ n_i\ w/2\tau \qquad (20)$$

where q = electronic charge, 1.6×10^{-19}

n_i = intrinsic carrier density of silicon at room temperature 1.4×10^{10}

w = space charge width

τ = minority carrier lifetime

If this is true, then the open circuit voltage degradation is dependent not only upon the decrease of the light generated current I_L, but also upon minority lifetime in the junction space charge region as well, according to Eqs. 16 and 20. This will be further discussed upon evaluation of the radiation damage data presented in Section 5.

2.4 Primary Drift Field Design Parameters

Since the above theories and relationships were being evolved during the course of the contract, the original drift field design parameters were, of necessity, partially intuitive and partially based on previous work. It was decided to fabricate drift field cells with a 40 to 50 micron drift region on the basis of theoretical calculations performed by Cheslow and Kaye (Ref. 2). Figure 3 shows that at 50 microns below the surface, 85 percent of incident air mass zero solar photons would be absorbed. Since a difference of 5 orders of magnitude of boron concentration is the maximum practical limit attainable, a

$$N = \int^{\lambda_G} N_0(\lambda)(1 - e^{-\alpha x}) d\lambda$$

$$N_0 = 3.3 \times 10^{17} = \int_0^{\lambda_G} N_0(\lambda) d\lambda$$

A SOURCE IS SUNLIGHT (m = 0)
B SOURCE IS 2800° K TUNGSTEN LAMP
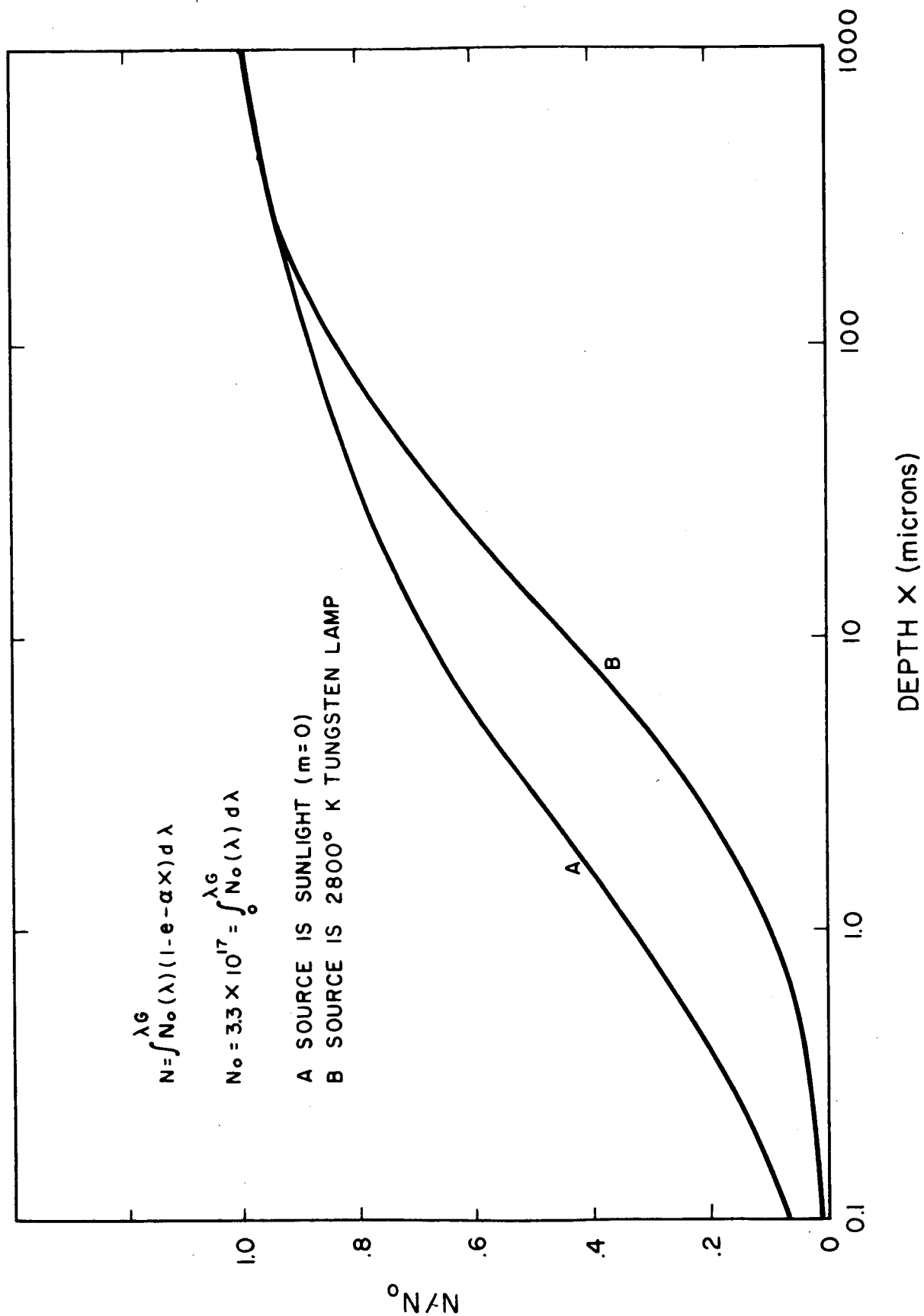
FIG. 3 NUMBER OF SOURCE PHOTONS ABSORBED ABOVE DEPTH X: SILICON

drift field with an average value of approximately 75 volts cm^{-1} could be attained. If the total drift field was made 100 microns long, 90 percent of incident air mass zero photons would be absorbed; however, now the average drift field would be between 30 to 35 volts cm^{-1}. These latter types of cells had already been made by Electro-Optical Systems, Inc., under NASA Contract NAS7-92 and had proven to be three to five times more radiation resistant than the best field free n-on-p cells available (Ref. 2). It was decided, therefore, to use the higher field configuration and lose the additional 5 percent of absorbed photons.

3. FABRICATION TECHNIQUES OF DRIFT FIELD CELLS

To develop methods of fabrication of the drift structures, several approaches were considered and attempted. Since 50μ thick silicon blanks are extremely fragile and would produce an extremely high breakage rate in any processing procedure, some method of applying backup structures on the reverse side of the active portion of the cell had to be employed. Three methods were attempted:

1. Alloying a low resistivity silicon blank on the boron predoped side of a high resistivity blank with aluminum and subsequently diffusing the boron and aluminum simultaneously into the high resistivity blank to form the drift field.

2. Epitaxially growing low resistivity silicon on a high resistivity blank containing a boron prediffused field.

3. Epitaxially growing carefully programmed resistivity silicon material forming the active field portion of the cell on a low resistivity substrate.

These are discussed in detail below along with attendant problems and results.

3.1 Aluminum Alloy-Diffused Approach

3.1.1 Alloying Process

In order to test the feasibility of the aluminum alloy diffused method of producing drift field cells, several preliminary runs were made. Both high (25Ω-cm) and low (<0.001Ω-cm) resistivity p-type 1 x 2 cm solar cell blanks were employed. The basic procedure was as follows:

1. Both resistivity type blanks were lapped and mechanically polished to remove surface damage.

2. Aluminum was vacuum evaporated on the polished side of both types.

4370-Final   18

3. The aluminum coated sides were sandwiched together and alloyed at $1{,}050^\circ$C in a nitrogen atmosphere for 10 minutes.

4. The sandwich structures were diffused for 20 hours at $1{,}200^\circ$C.

5. The high resistivity side of the sandwich was then lapped to within 100 microns of the aluminum interface.

6. The lapped surface was polish-etched to within 50 microns of the aluminum interface.

7. Phosphorous was diffused into the top surface at 930°C forming a junction approximately 0.5 micron below the surface.

8. The grid pattern was applied using photolithographic techniques and silver plating.

9. The cell was masked on top and bottom and the edges etched to clear the junction.

10. Silicon monoxide was vacuum evaporated on top surface to produce an antireflection coating.

3.1.2 Fabrication Problems and Results

The first run was fabricated according to the above procedure. The thickness of the evaporated aluminum was approximately 1 micron, and the slices were diffused with the high resistivity side down on the diffusion boat. Two facts became apparent during steps 5 and 6:

1. In the course of the diffusion process, the aluminum alloyed deep into the high resistivity blanks along what appeared to be dislocated areas. The appearance of the surfaces of most of the cells of the first run after the etch process in step 6 was that of nonuniformities in a more or less geometric pattern.

2. Cracking around the edges of the high resistivity slices after the lapping and etching steps, and in some samples, complete disassociation of the two blanks.

The cause of the first is thought to be that, as the slices cooled in the furnace upon withdrawal, the top portion cooled first, thus causing the aluminum to segregate downward toward the hotter portion of the sandwich. The latter runs were made with the low resistivity slices on the bottom.

The cause for the second occurrence is primarily due to the fact that in the polishing procedure of step 1, the edges tended to round on both slices, and in subsequent alloying the aluminum-silicon alloy tended to pull inward from the edges of the sandwich, thus leaving gaps around the edges.

Another fact which became evident upon evaluation of the diffused structures according to the double angle lap method explained in Subsection 3.1.3 of this report, was that no apparent boron doping of the graded region from the low resistivity wafer ensued as a result of the 20-hour diffusion used to form the drift field structure. However, the angle sections did show that the tail of the aluminum diffusion did extend approximately 50 microns into the high resistivity material, although no accurate quantitative estimate of the doping profile could be obtained due to the high concentration aluminum alloy apparent along the dislocations. To verify the doping level at the subsequent p-n junction, another evaluation method was resorted to as explained in Subsection 3.1.3 of this report.

In view of this, two succeeding runs were split into two portions; in the first portion boron was deposited into the polished face of the high resistivity blanks with a concentration of approximately 1×10^{20} atoms cm^{-3} prior to the aluminum evaporation (step 2 of the procedure). The other portion of both runs was fabricated without the aid of this boron predeposit. Unfortunately, the edge-cracking problem was still significant and the majority of the samples was lost in steps 5 and 6 of the procedure.

As a result of these problems, only three cells remained which were capable of any significant output. The results of

tungsten and sunlight output measurements are discussed in Section 4 of this report. These cells were submitted to GSFC as the first samples.

In order to alleviate the edge-cracking and etching problems associated with the 1 x 2 cm, larger slices of the same resistivity material were used (0.0004Ω-cm and 25Ω-cm). Two separate approaches were employed, and after diffusion, alloying, and grid application, the cells were cut to size using ultrasonic cutting equipment.

In the first approach, a deposit of boron was made on 25Ω-cm p-type material with a surface concentration of approximately 3 x 21 atoms/cm^3. Aluminum was vacuum evaporated on this boron-doped surface and the corresponding surface of a low resistivity p-type slice. The two aluminized surfaces were then placed together, and the resulting sandwich structure placed in an alloying furnace at 1,050°C in a nitrogen atmosphere. After alloying, the structures were diffused at 1,200°C for a period of 20 hours. The structures were lapped and chem-polished to a distance of 50μ above the aluminum silicon interface. At this time, it was noticed that relatively large portions of aluminum formed balls and alloyed into the high resistivity material. Consequently, all cells made from these structures were shortcircuited.

The second approach was to predeposit boron on the side of the high resistivity slices and diffuse the boron alone to a depth of approximately 50 microns before the aluminum deposition. Aluminum was then vacuum deposited and alloyed as in the first approach; however, the samples were not diffused at the higher temperature, the boron prediffusion being used to form the drift field structure. After lapping and chem-polishing the samples to a point 50 microns from the aluminum silicon interface, phosphorous was diffused on this surface, the grid structure applied, the cell ultrasonically cut to size, masked, and the edges etched to clear the junction. Of the six samples run in this experiment, two cells were not shorted. The reason for the inability to etch the junction on the other four cells is not

fully understood at present. It is thought that an insufficient amount of aluminum was deposited, causing an inhomogeneous alloy formation, some chipping and disassociation of the alloy structure being evident. As a result, during the phosphorous diffusion, the phosphorous vapor entered between the slices. It is interesting to note that the two nonshorted cells showed the least amount of chipping.

These two cells, and a third cell fabricated from 1 x 2 cm blanks, were submitted to Goddard Space Flight Center for evaluation as the second group of samples. Their electrical characteristics are noted in Section 4 of this report.

3.1.3 Dopant Concentration Evaluation

Three different methods are readily available and were used for the evaluation of drift fields in the aluminum alloy-diffused structures.

In the first method, sample structures were fabricated and a resistivity profile made by successive etching and measuring with a 4-point probe at approximately 5μ intervals through the drift field region. This, however, was not a suitable method for evaluation of the aluminum alloy diffused samples. The thin aluminum layer, sandwiched between the high and low resistivity silicon slices, provided too low a conduction path for current supplied by the 4-point probe apparatus, which resulted in so low a signal level that the change in the integrated resistance of the sample, due to the removal of a thin layer by etching, was not detected.

A second method, described by Sils and Wang (Ref. 6), was attempted with some success. The method consists primarily of lapping and polishing a shallow angle (1° to 5°) on the surface of the sample in question, and diffusing the opposite impurity dopant onto the original surface and angle. After diffusion, a second angle is lapped and polished normal to the first angle and stain etched. The difference in discolorations between the n and p materials clearly defines their boundary with a resultant "panoramic view" of the resistivity profile.

Knowledge of the surface concentration of the second diffusion, the initial concentration of the diffusant used to form the graded base structure, and the concentration of dopant in the high resistivity material, into which both diffusants entered, provide convenient and adequate calibration points when the sample is photographed with interference microscopy.

A third method was attempted with much better success. Thomas, et al., (Ref. 7) have shown the usefulness of capacitance versus reverse voltage measurements on junction devices fabricated on epitaxially grown substrates to determine the auto-doping profile in such substrates. The method is based on the fact that the slope of $1/C^2$ versus the applied reverse voltage is a simple function of the doping concentration adjacent to the junction.

The procedure is as follows: the capacitance is measured at some given reverse voltage. The dial setting on the capacitance bridge is detuned by a small increment, approximately 1 to 2 percent. The voltage is then changed to rebalance the capacitance bridge and the voltage noted. This gives $\Delta C/\Delta V$ or approximately dC/dV which corresponds to the slope of the capacitance versus voltage function at the given C and V values for the particular diode. With appropriate correction for diode area, the doping concentration and the depth at which the measurement was made can be determined from a nomograph published in Ref. 4. However, since the published nomograph encompasses only three orders of magnitude of dC/dV, a larger, expanded model encompassing eight orders of magnitude was constructed to evaluate the present measurements.

The third method was tested on a sample of an aluminum alloy-diffused structure with a boron predeposit. On one portion of the sample, the junction was at 50 microns above the aluminum alloy region, and on the other, at 30 microns. The results and the theoretical curve for the simultaneous diffusion of boron and aluminum are shown in Fig. 4. It is evident that the actual concentration profile
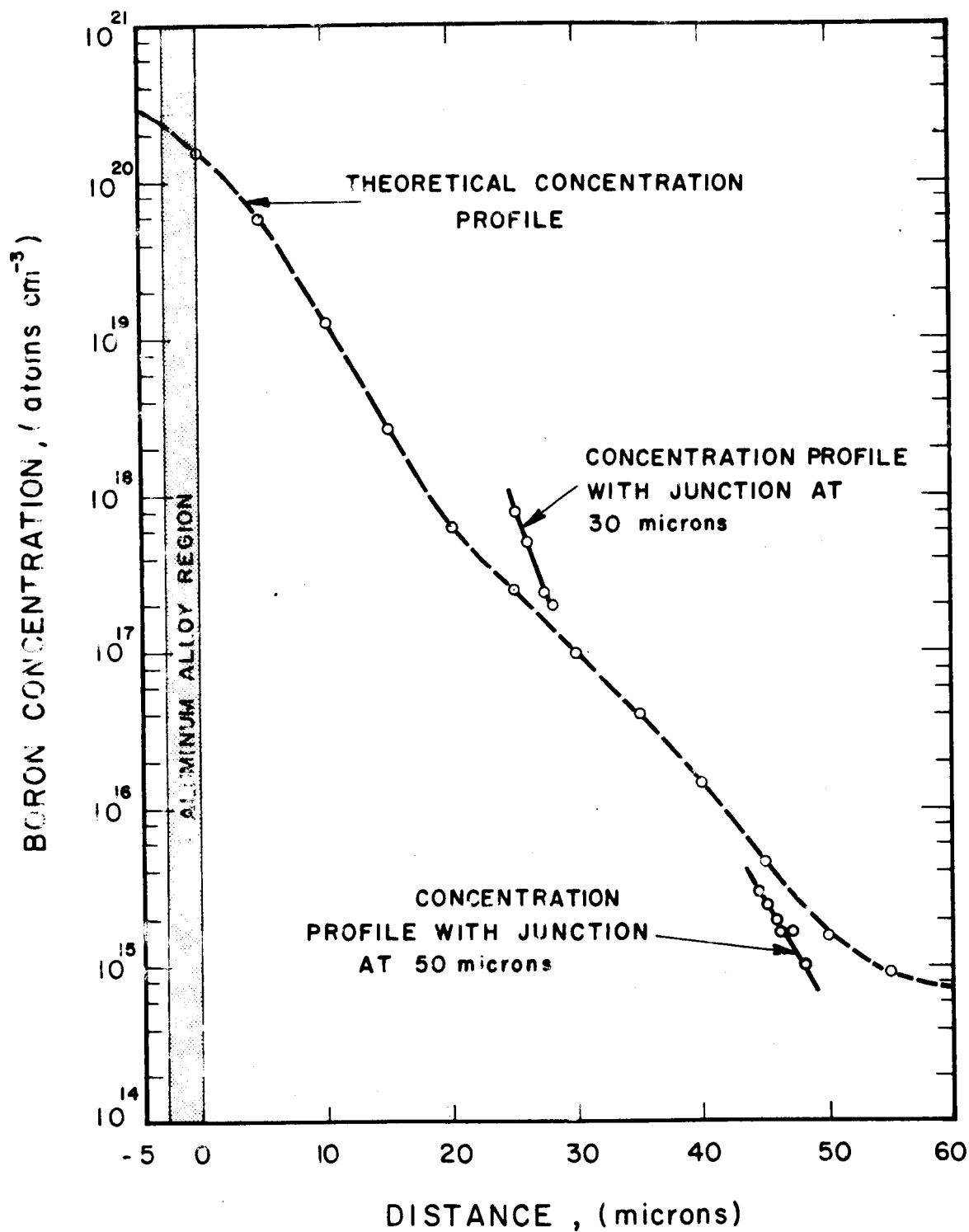
FIG. 4 RESULTS OF CAPACITANCE MEASUREMENTS ON ALUMINUM ALLOY –
DIFFUSED STRUCTURES

follows the theoretical fairly closely, especially at the point approximately 25 microns from the aluminum alloy region where the theoretical curve predicts a higher boron concentration. It is interesting to note the increase in slope of the experimental curve in this region.

3.2 Reverse Epitaxial Approach

3.2.1 Fabrication Process

The reverse technique procedure was as follows:

1. Boron was predeposited on a polished side of 25Ω-cm 1 x 2 cm solar cell blanks and diffused for a period of 96 hours at 1,250°C, to a depth of 55 to 60 microns.

2. Between 0.005 inch to 0.007 inch of low resistivity p-type silicon was epitaxially deposited on top of this diffused drift field.

3. The opposite side of the cells was lapped and chem-etched to a point 55 microns from the epitaxial boundary.

4. Phosphorous was diffused to form the junction.

5. The grid structure was applied by photolithographic means and silver plating.

6. The cells were masked and the edges etched to clear the junction.

7. Solder was applied to the grids and silicon monoxide anti-reflection coatings evaporated to the top surface.

3.2.2 Problems and Results

The first attempts to fabricate cells from material with growths 0.007 to 0.012 inch thick gave cells with poor I-V characteristics. Impurities were discovered in the epitaxial gas stream, which caused large quantities of stacking faults in the growths. This imperfect material, having a slightly different coefficient of expansion than the good silicon on which the epitaxial layer was grown, produced dislocations and strains in the substrate material through plastic deformation. This was first evidenced by low short-circuit

currents and the inability to obtain good characteristic curves on fabricated cells. A subsequent dislocation etch in a solution of:

CrO_3	20 grams
HF (48%)	45 ml
H_2O (distilled)	40 ml

for 45 seconds on the top surfaces of the shorted or poor characteristic cells showed large numbers of dislocation etchpits in elongated clusters along with single pits. The same etch performed on control cells fabricated from the same starting material produced no etchpits, either in clusters or singly. After the epitaxial impurity situation which was due to a faulty valve was rectified, much better quality growths were obtained. Cells fabricated from these structures had much better I-V characteristic curves, and had dark leakage currents of less than 50 microamperes at 1 volt reverse bias.

3.2.3 Dopant Concentration Evaluation

Samples from separate long boron diffusion runs were evaluated by means of successive four-point probe and etching steps. The conductivity and consequent boron concentration can be determined from the following relation:

$$\sigma_n = \left[\frac{1}{R_1} - \frac{1}{R_2} \right] \frac{1}{X_n} \tag{21}$$

where σ_n is the average conductivity of the nth layer, R_1 and R_2 are the sheet resistances as measured by the 4-point probe before and after the removal of the nth layer and X_n is the thickness removed. The results are shown in Fig. 5.

The theoretical curve was obtained by solution of the error function relation:

$$N_x = N_s \, \text{erfc} \left[\frac{x}{2\sqrt{Dt}} \right] \tag{22}$$

where

N_x = concentration at distance x

N_s = surface concentration

D = diffusion constant in cm^2/sec of boron in silicon at $1,250^{\circ}C$

t = time in seconds

The surface concentration N_s was obtained by sheet resistance measurements on an n-type control slice and incorporation of Irvin's data (Ref. 8). The reason for the obvious discrepancy between theory and experiment is not known at this time.

Figure 6 shows the results obtained on a subsequent sample, this being representative of the other samples. Because of the good agreement with theory of these results, greater confidence was placed in this method.

3.3 Front Epitaxial Approach

Two methods of epitaxial deposition of silicon were attempted:

1. The hydrogen reduction of silicon tetrachloride by means of the overall reaction:

$$Si\ Cl_{4(1)}\ \&\ 2H_{2(g)} \overset{\Delta}{\underset{\leftarrow}{\rightarrow}} Si_{(s)}\ \&\ 4H\ Cl_{(g)} \tag{23}$$
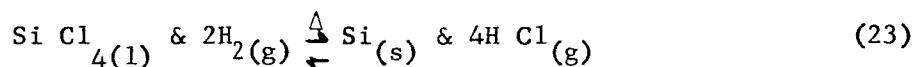
the halide being introduced into the reaction chamber as a vapor by bubbling controlled amounts of H_2 through the liquid.

2. The pyrolysis of silane by the reaction:

$$SiH_{4(g)} \overset{\Delta}{\rightarrow} Si(s) + 2H_2 \tag{24}$$

3.3.1 Hydrogen Reduction of Silicon Tetrachloride

The epitaxial system was reconstructed to insure its being leak-free. When not in use it was kept under constant vacuum, aiding moisture-free operation. The results of the first growths on the reconstructed system are listed in Table I. It is apparent that after Run No. E-14, the majority of the p-type contamination was leached out of the system, since the growths were doped by auto-doping

TABLE I

RESULTS OF FIRST EPITAXIAL RUNS ON NEW ALL-PYREX SYSTEM

| Run No.	Temperature	Rate	Total Thickness	Remarks
E-10	1200°C	0.15μ/min	1 to 2μ	P, low resistivity single crystal
E-11	1275°C	0.7 μ/min	8μ	P, low resistivity single crystal
E-12	1280°C	2.0 μ/min	60μ	P, medium resistivity polycrystal
E-13	Run aborted			
E-14	1200°C	0.6 μ/min	10μ	N type on N substrate Good quality single crystal
E-15	1290°C	0.9 μ/min	27μ	N type on N substrate Good quality single crystal
E-16	1290°C	0.85μ/min	25μ	P type on P type substrate. Good quality single crystal
E-17	1290°C	0.85μ/min	75μ	N type on N type substrate. Good quality single crystal
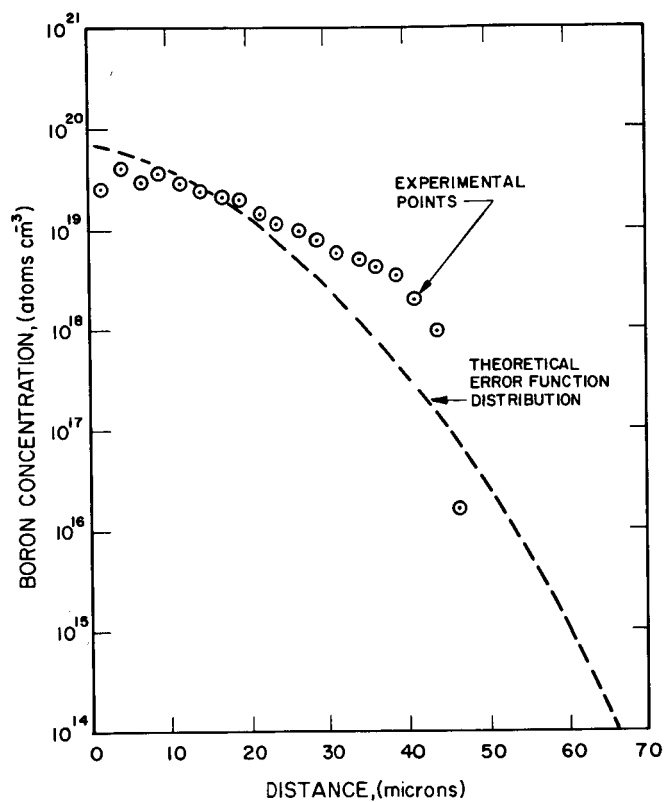
FIG. 5

THEORETICAL AND EXPERIMENTAL RESULTS
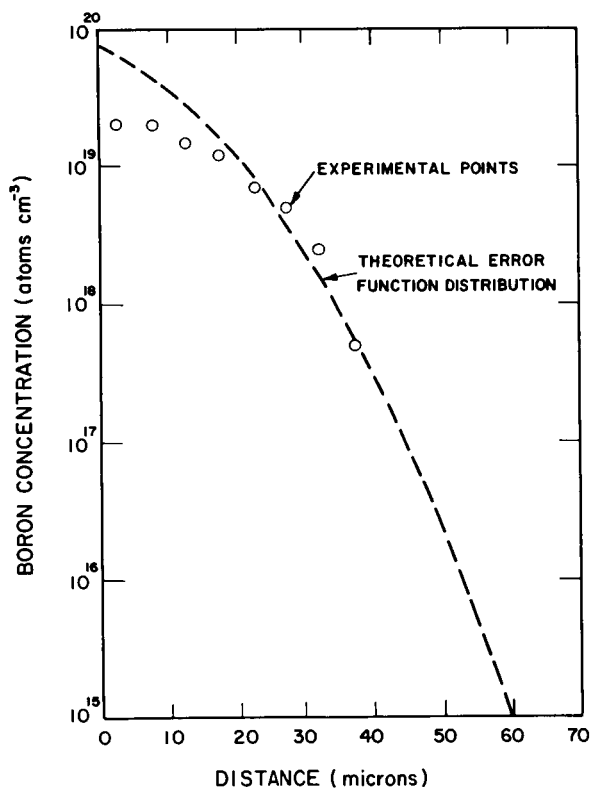OF BORON DIFFUSION INTO 25 ohm-cm P
TYPE SILICON

FIG. 6

DRIFT FIELD EVALUATION BY 4-POINT
PROBE METHOD

from the growth substrate. No extraneous doping of either type was used and the growths were performed from a semiconductor grade $SiCl_4$ source. Runs No. E-10 and E-11 were not good quality single crystal growths, polycrystalline patches and crystallites being visible to the unaided eye.

Runs No. E-14, E-15, E-16, and E-17 were excellent growths. They were evaluated by immersing in the above mentioned solution and etched for 45 seconds. Figure 7 (a, b, c, and d) shows the results of this etch on samples E-14, E-15, E-16, and E-17 respectively. These photomicrographs were made at 400X magnification and represent areas of 6×10^{-4} cm^2.

The equilateral triangles are indications of stacking faults, the larger triangles indicating stacking faults occurring at or very near the substrate-growth interface, and the smaller ones (see Figs. 7b, 7c) indicating faults occurring higher in the growth region. These triangles represent the bases of inverted tetrahedra, the apices of which originate at the stacking fault origin. There exists a relationship whereby the height of a tetrahedron can be related to the length of a side (Ref. 9):

$$height = length \ of \ side \times sin \ 54.7^{\circ}$$

By this method a fairly accurate approximation of the growth thickness can be obtained even though angle-lapping and stain-etching techniques fail such as in the cases of p-on-p or n-on-n type growths.

Runs No. E-14 to E-17 were performed with a hydrogen to silicon tetrachloride mole-ratio of approximately 300 with an average gas velocity through the reactor of 220 cm/min. This higher flow rate, although probably reducing the growing efficiency, tends toward more uniform total growth over a longer length (Ref. 10). The heating apparatus consists of a carbon block coupled to an rf generator, with heat transfer to the growth substrate accomplished with a quartz flat.

CONTENTS

a   (Run E-14)

c   (Run E-16)

b   (Run E-15)

d   (Run E-17)

FIG. 7   PHOTOMICROGRAPHS OF EPITAXIAL RUNS E-14 THROUGH E-17

Since the system at this time was growing relatively pure silicon, it was proposed to fabricate the first samples of epitaially grown drift field cells via the front surface growth method. Experimental runs were performed to evaluate the quality and resistivity of growths on low resistivity (0.0004Ω-cm) boron doped material. The results of the more significant runs are shown in Table II; additional runs, not listed, were performed for c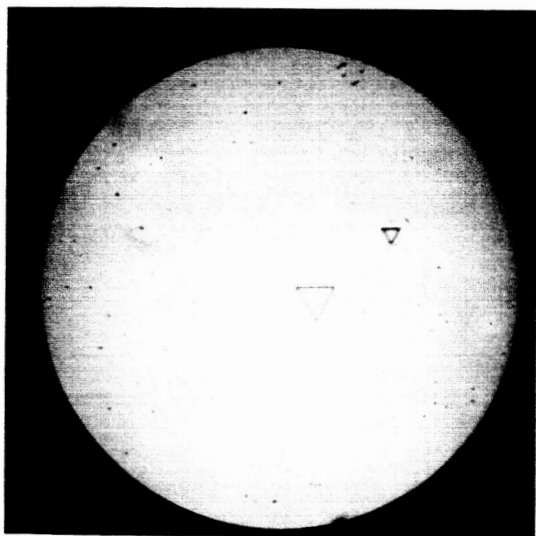alibration of temperature, flow rates, etc. Since the "front" active portion of the solar cell should be made of low dislocation, medium resistivity material, the epitaxial system was now considered adequate for use in the fabrication of such structures.

The lower growth temperatures were considered necessary to minimize auto-doping effects from the low resistivity substrates. Growth rates were kept constant during all runs, approximately 1μ/min. The thicknesses of the runs noted were 50 microns, except Run No. E-25 which was 27 microns. The doping level was determined by capacitance measurements on diodes fabricated on the grown surface. In addition, a sample of Run No. E-19 was beveled at a 1$^{\text{o}}$ angle, and capacitance measurements made on diodes constructed on this bevel. This showed the doping level to be constant in the top 25 microns of the growth, being approximately 2 to 3 x 10^{16} atoms of boron/cm^{3}.

Runs No. E-19 through E-25 were made on at most two 1 x 2 cm blanks at one time on a carbon heater 1 x 2 inches. To increase the capacity of the system in which more blanks could be prepared at one time, it was decided to fabricate a larger carbon susceptor, having a heated surface area of approximately 7 in^{2}. Subsequent runs made employing this susceptor produced slices with growths on the order of 0.1Ω-cm p-type although of good single crystal quality. Higher resistivities could not be grown, although four runs were made. The exact reason for this is unknown at this time, although it is thought that the higher doping levels are a result of increased auto-doping from the increased number of slices, and doping from the larger surface area of

TABLE II   RESULTS OF EPITAXIAL RUNS ON 0.0004Ω-cm P-TYPE SUBSTRATES

Run Number	Growth Temperature	Boron Concentration as evaluated by capacitance measurements	Resistivity	Remarks
E-19	$1290^{\circ}C$	2 to 5 x 10^{16} atoms/cm^3	.5 to 1Ω cm	few stacking faults, moderate dislocations
E-21	$1240^{\circ}C$	1.3 x 10^{16} atoms/cm^3	1.5Ω cm	few stacking faults, moderate dislocation.
E-22	$1210^{\circ}C$	3.5 x 10^{15} atoms/cm^3	4Ω cm	few stacking faults moderate dislocations
E-25	$1210^{\circ}C$	- -	- -	no stacking faults, few dis-locations

silicon deposited on the carbon heater. As a result of this diffi-
culty, it was decided to attempt front epitaxial growths employing
silane.

3.3.2 Pyrolysis of Silane

The experiments were based on the work reported by
Mayer and Shea on the pyrolysis of silane (Ref. 11). Results were in
fair agreement with their findings as far as the effects of hydrogen-
silane ratios, total gas velocities, and substrate temperatures on
growth rates (see Table III).

The apparent decrease of growth rate with time under
identical flow, silane ratio, and temperature conditions, as evidenced
by runs E-41, E-42, and E-43, was thought to be due to the formation
of a fine web of dendritic silicon at the head of the slice-carrying
apparatus. After approximately 15 minutes of growth, this dendrite
growth became appreciable, and the gas flowed through this web before
reaching the substrates. As the growth progressed and the dendrites
became larger, more silicon area was exposed to the silane contained
in the gas stream, decomposing it and, thus, reducing the amount of
silane available at the desired substrate. This condition was allevi-
ated by a redesign of the substrate holder, with a view toward deter-
ring the dendritic growth.

The quality of the grown layers, however, was not
satisfactory. Large numbers of stacking faults appeared on the epitax-
ially grown surfaces when etched with the CrO_3-HF etch. The number of
stacking faults in the present growths was substantially higher than
on similar growths formed by the hydrogen reduction of silicon tetra-
chloride. This is possibly due to the fact that, in the halide reduc-
tion process, the growth process is reversible, (see Eq. 23) and a
certain amount of "etch back" of the grown layer occurs, keeping the
number of stacking fault sites at a minimum. Since the pyrolysis of
silane reaction is not reversible at the temperature in question,
(see Eq. 24) this "etch back" does not occur and the number of stacking
fault sites increases.

TABLE III

CONDITIONS AND RESULTS OF INITIAL SILANE GROWTH RUNS

Run Number	Hydrogen to Silane Ratio	Mixture Velocity Through Reactor (cm min^{-1})	Growth Temperature ($^{\circ}$C)	Growth Rate (min^{-1})	Total Growth Time (min)
E-37	650:1	230	1215	0.28μ	40
E-38	800:1	170	1215	0.38μ	30
E-39	500:1	170	1215	0.38μ	30
E-40	500:1	170	1250	0.4μ	30
E-41	500:1	340	1220	0.7μ	15
E-42	500:1	340	1220	0.65μ	35
E-43	500:1	340	1220	0.5μ	50

P-N junction devices fabricated from these highly imperfect epitaxial crystalline layers exhibit poor I-V characteristics. Figure 8 shows the characteristic under forward and reverse bias of a diode fabricated from a 1 by 2 cm blank included in run E-42. Several successive edge etchings did not increase the forward-to-back ratio of the trace; therefore, it can be presumed that the leakage current originates in the bulk epitaxial layer as bulk recombination current. Also, an attempt to determine the impurity profile of the epitaxial layer of run E-42 by the fabrication of diodes on etched steps and subsequent capacitance measurement failed because of the extremely poor quality of the diodes.

Subsequent runs were attempted and because of the tendency toward dendritic growth with the silane process, efforts were primarily made toward impeding this tendency by altering the system geometry and using silicon slabs as slice carriers. The rates of dendritic growth were reduced. However, after growths of greater than 25μ, dendrites begin to form leaving the surfaces of the samples rough.

With no doping during growth, resistivities of 5 to 15Ω-cm p-type have been obtained. This boron dopant is thought to come from the Pyrex glassware, since undoped silane growths have been reported to be predominantly high resistivity n-type.

3.4 Comparison of the Three Approaches

Of the three approaches used, the reverse epitaxial technique yielded the best results and the majority of the cells submitted to GSFC for radiation damage evaluation were fabricated in this manner. The technique is not extremely critical and is conducive to tighter control since:
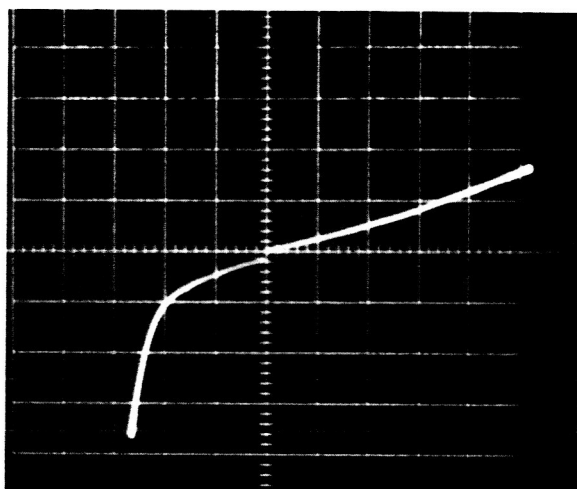
25 ma PER DIVISION

0.25 VOLTS PER DIVISION

FIG. 8 I-V CHARACTERISTIC OF SOLAR CELL
FABRICATED FROM RUN E-42

1. Formation of the drift field impurity gradient is performed by solid state diffusion, the only controllable quantities being surface concentration of the dopant, time and temperature. These are at this time much investigated and accepted aspects of solid state technology.

2. The placing of the backup material on the back side of the cell is done by an epitaxial process in which the control of the level of doping impurity is noncritical. This is in direct opposition to the front epitaxial approach in which the epitaxial layer forms the drift field portion of the cell and in which the doping level control is extremely critical.

3. The removal of the undesired portion of the active portion of the cell is performed by readily controllable mechanical lapping and chemical etching techniques.

Although the aluminum alloy-diffused method yielded some usable cells, the problems encountered in the alloying procedure tend to indicate that more investigation would of necessity have to be performed if this technique is considered in the future. Since the drift field in this device is also diffused, and no epitaxial process is necessary for fabrication of the passive backup layer, the remaining problem of the alloying procedure is the only critical factor in future considerations.

The distinct advantage of the front epitaxial approach is the ease of varying the drift field configuration by proper control of the dopant concentration during growth. This is not impossible in either of other two methods in which the drift field is formed by diffusion and a varying drift field can be obtained by suitable programming of dopant concentration diffusion time and temperature. However this appears more difficult than the front epitaxial approach. On the other hand, since the epitaxial layer forms the active portion of the cell, it must of necessity be of excellent crystalline quality, and the dopant concentration strictly controlled.

4. ELECTRICAL TESTS

The I-V characteristics under tungsten illumination of the first aluminum alloy-diffused sample cells submitted to Goddard Space Flight Center for evaluation are shown in Fig. 9. The conditions of their fabrication and results of sun measurements are shown in Table IV. The sun measurements were made using an Eppley collimated pyrheliometer to monitor the incoming energy and a Boonton 0.1 percent milliammeter to measure the short circuit current. The extrapolation of the short circuit current I_{SC} to 100 mw/cm^2 incoming energy was performed as a simple ratio, assuming the relation of I_{SC} to incoming intensity to be linear. The cause of the relatively high percentage increase of the I_{SC} in sunlight over tungsten was thought to be primarily due to a combination of the increased effectiveness of the drift field, the theory presented in Fig. 3, and the silicon monoxide antireflection coatings which were optimized for sunlight rather than a 2,800°K tungsten source.

The I-V characteristics of the second group of samples submitted for evaluation are shown in Fig. 10. No sunlight measurements were performed upon the suggestion of the contract monitor, who indicated that spectral response measurements would be more meaningful at that time. Since the spectral response measuring equipment was not in operation at Electro-Optical Systems at that time, Goddard Space Flight Center offered to perform the measurements.

Figure 11 shows the output characteristics of the first samples of reverse epitaxial cells submitted to Goddard Space Flight Center for evaluation. Unfortunately, measurements in sunlight could not be made due to bad weather conditions.

Subsequent samples of drift field cells fabricated via the reverse epitaxial technique are listed in Tables V, VI and VII. Cells with the
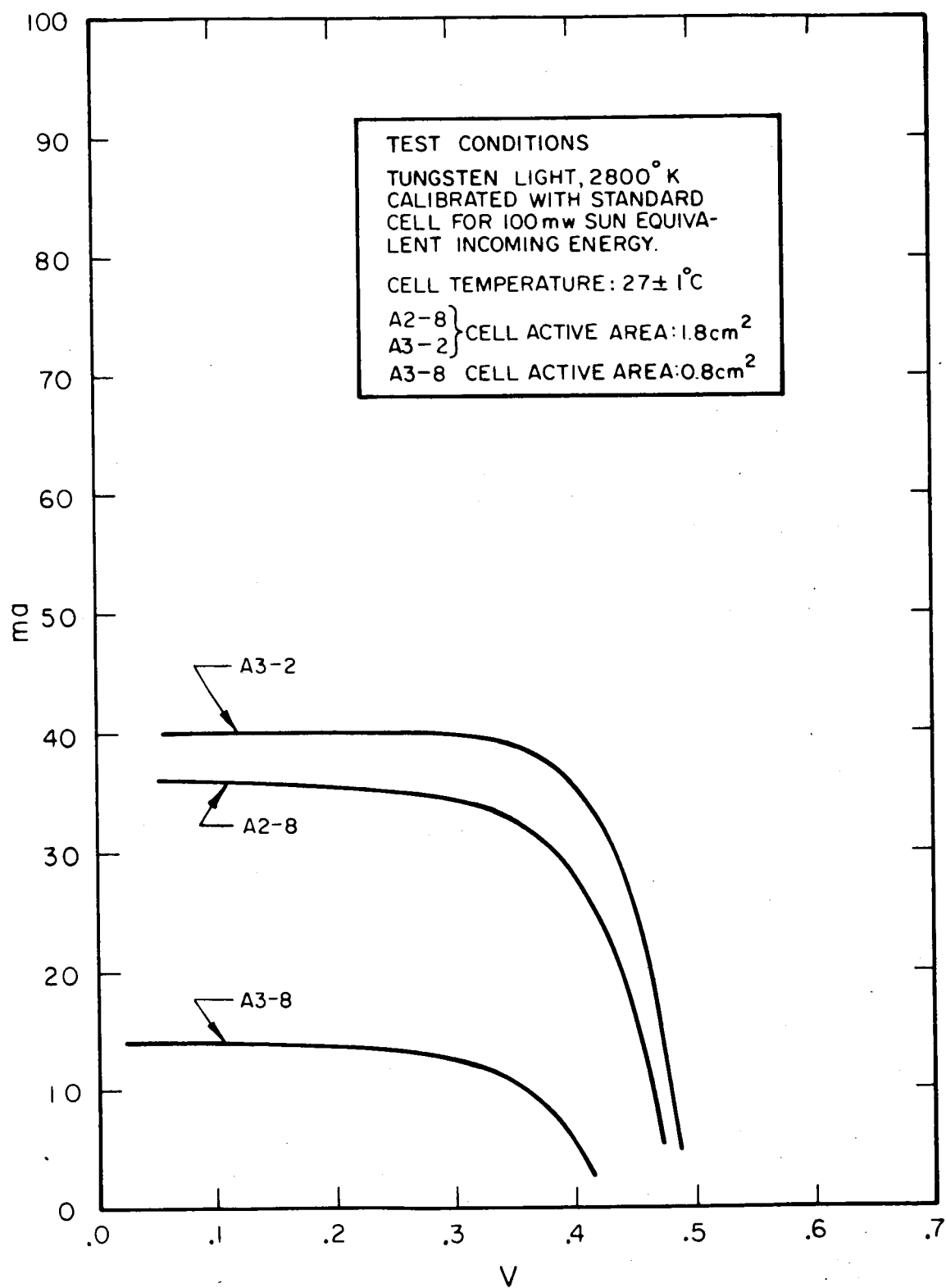
FIG. 9 I-V CHARACTERISTICS OF FIRST SAMPLE CELLS UNDER TUNGSTEN
ILLUMINATION

TABLE IV

TEST DATA ON FIRST SAMPLES

	Cell No.		
	A2-8	A3-2	A3-8
Efficiency in tungsten light	6.2%	7.9%	4.2%
I_{SC} in tungsten at 100 mw/cm^2 equivalent in ma	36.0	40.0	14.2
Incoming sunlight energy, in mw/cm^2	89.4	89.5	89.5
I_{SC} in sunlight in ma	36.0	38.0	14.5
I_{SC} in sunlight corrected to 100 mw/cm^2 incoming energy in ma	40.5	42.5	16.2
Apparent percentage increase in sunlight over tungsten	11.0	6.0	12.0
Fabrication condition	No boron predeposit	Boron pre-deposition high resistivity slice	No boron predeposit
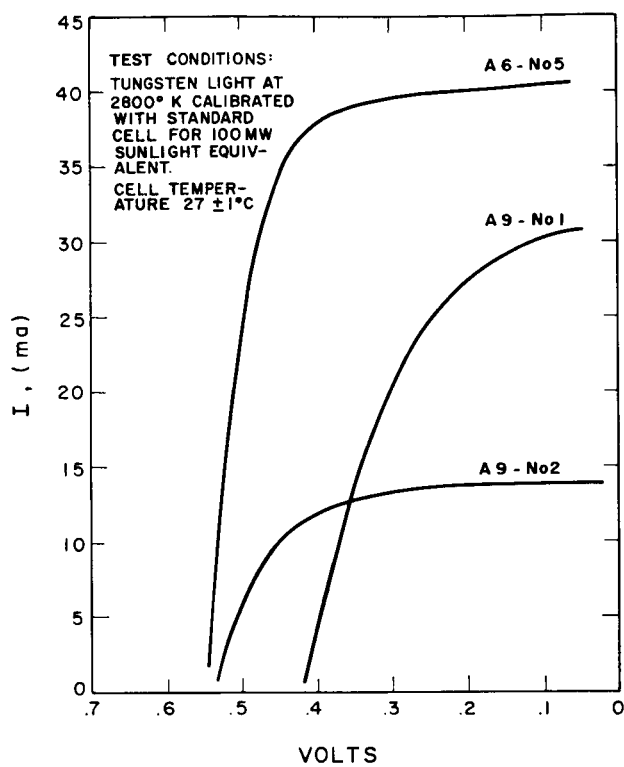
FIG. 10

I-V CHARACTERISTICS OF SECOND SAMPLE
CELLS UNDER TUNGSTEN ILLUMINATION
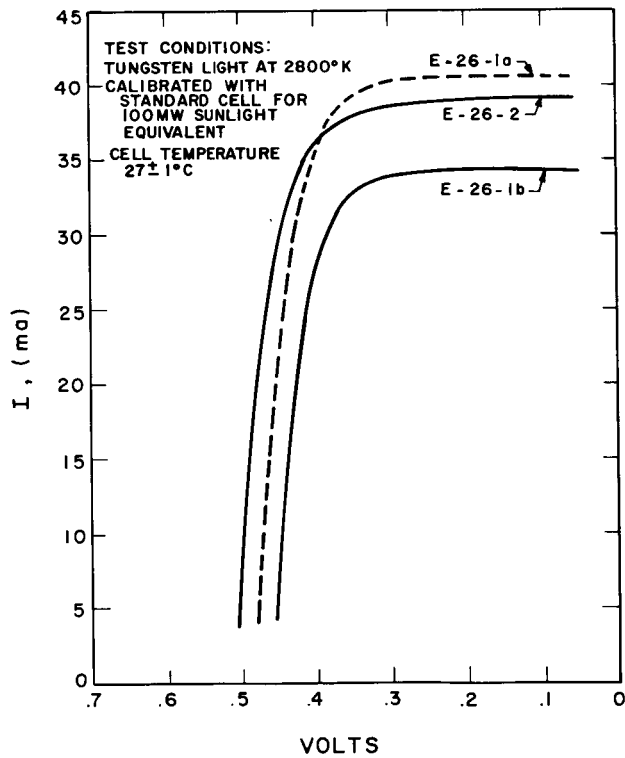
FIG. 11

I-V CHARACTERISTICS OF EPITAXIAL
CELLS UNDER TUNGSTEN ILLUMINATION

TABLE V

RESULTS OF TUNGSTEN SUNLIGHT MEASUREMENTS

Cell Number	Sunlight Incoming Energy in mw cm^{-2}	I_{sc} in ma cm^{-2}	I_{sc} Extrapolated to 100 mw cm^{-2} Incoming Energy in ma cm^{-2}	I_{sc} in Tungsten Calibrated with Standard Cell in ma cm^{-2}
E 26-3A	86.0	17.5	20.3	17.2
E 26-3B	86.0	15.3	17.8	13.6
E 26-3C	86.0	16.9	19.7	17.2
E 26-4A	86.5	19.4	22.5	19.4
E 26-4B	86.0	19.4	22.6	19.1
E 26-4C	86.7	12.2	14.1	9.2
E 26-4D	87.2	17.8	20.3	17.8
E 26-5	87.2	12.9	14.8	10.0

TABLE VI

SUNLIGHT AND TUNGSTEN MEASUREMENTS OF SUBMITTED SAMPLE CELLS

Cell No.	Incoming Energy in mw cm^{-2}	I_{sc} in ma cm^{-2}	I_{sc} at 100 mw^{-2} in ma cm	I_{sc} Tungsten in ma mc^{-2}
C-1A	85.5	19.5	23.7	25.1
C-1B	84.0	20.0	24.7	25.4
C-1C	83.0	20.5	24.9	27.0
C-1D	82.0	21.6	26.5	27.0
C-1E	83.0	18.4	22.2	24.1
C-1F	82.0	17.3	21.1	21.9
C-1G	84.0	19.5	23.2	24.9
E33-1A	84.0	17.3	21.1	17.8
E33-1B	84.5	16.2	19.5	15.1
E33-2A	85.0	11.4	13.5	9.5
E33-2B	86.0	14.6	16.8	13.8
E33-2C	86.0	15.7	18.4	17.3
E33-3A	86.0	13.0	15.1	10.3
E33-3B	86.0	16.2	18.9	14.6
E34-1B	84.5	16.2	19.4	15.4
E34-1C	84.5	21.2	25.1	22.9
E34-1D	84.5	17.8	21.1	17.3
E34-1E	84.0	20.0	23.8	22.2

TABLE VII

SUNLIGHT, TUNGSTEN AND CONVERSION EFFICIENCY DATA ON LAST GROUP OF SUBMITTED CELLS

Cell Number	Incoming sunlight energy in mw cm^{-2}	I_{sc} in ma	I_{sc} at 100mw in ma cm^{-2}	I_{sc} Tungsten in ma cm^{-2}	Sunlight conversion efficiency in percent
*E-34-3A	105.0	40.0	20.54	23.0	7.3
*E-34-3B	99.5	37.0	20.05	22.0	7.0
*E-34-3C	99.0	35.0	19.08	18.9	6.5
*E-34-3D	99.5	36.5	19.78	19.7	6.5
*E-34-3E	99.5	38.5	20.86	23.2	7.6
E-34-3F	100.0	21.0 (1X1)	24.70	25.4	9.1
*E-34-3G	99.5	35.0	18.97	19.7	6.6
*E-35-1A	99.5	40.0	21.72	22.1	7.6
*E-35-1B	100.0	39.0	21.08	22.1	7.5
*E-35-1C	100.0	41.0	22.16	23.5	8.0
*E-35-1E	100.0	39.0	21.08	21.9	7.6
*E-35-1F	100.0	39.0	21.08	20.8	7.7
*E-35-2A	102.0	40.0	21.18	20.8	7.1
*E-35-2B	102.0	42.0	22.21	21.9	7.3
*E-35-2C	102.0	43.5	23.02	23.2	9.3
*E-35-2D	102.0	44.0	23.29	23.2	9.0
*E-35-2E	102.0	41.5	21.94	21.9	7.0
*E-35-2F	102.0	40.5	21.45	21.1	9.1
*E-35-3A	103.0	37.5	19.76	19.5	8.3
E-35-3B	102.0	37.0	19.56	18.4	8.1
E-35-3C	102.0	34.5	18.27	18.4	Bad Curve

TABLE VII (contd)

SUNLIGHT, TUNGSTEN AND CONVERSION EFFICIENCY DATA ON LAST GROUP OF SUBMITTED CELLS

Cell Number	Incoming sunlight energy in mw cm^{-2}	I_{sc} in ma	I_{sc} at 100 mw in ma cm^{-2}	I_{sc} Tungsten in ma cm^{-2}	Sunlight conversion efficiency in percent
*E-35-3D	102.5	40.5	21.35	22.2	8.5
E-35-3E	102.5	36.0	18.97	18.6	6.5
E-35-4A	102.5	41.5	21.83	23.5	7.6
*E-35-4B	102.0	41.5	21.94	23.0	8.0
*E-35-4C	102.0	42.0	22.21	23.5	7.9
E-35-4D	102.5	42.5	22.37	23.4	8.0
E-36-1A	102.5	14.5 (IXI)	16.58	15.3	6.6
E-36-1B	103.0	14.5 (IXI)	16.47	14.1	Bad Curve
E-36-2A	103.0	16.5 (IXI)	18.82	17.6	8.0
E-36-2B	103.0	15.5 (IXI)	17.64	18.8	Bad Curve
E-36-2C	102.0	15.5 (IXI)	17.76	16.7	6.5
*E-36-3A	102.5	17.5 (IXI)	20.00	19.5	8.0
*E-36-3B	102.5	17.5 (IXI)	21.17	21.8	8.1
*E-34-2A	104.0	42.0	21.78	23.2	7.9
*E-34-2B	103.5	41.5	21.62	21.9	8.0
*E-34-2C	104.0	41.5	21.56	22.7	7.4
*E-34-2D	104.0	43.0	22.32	24.1	7.3
*E-34-2E	104.5	43.2	22.32	23.4	8.6
*E-34-2F	103.5	42.5	22.16	23.2	7.9
E-34-2G	104.0	44.5	23.08	23.0	Bad Curve

TABLE VII (contd)

SUNLIGHT, TUNGSTEN AND CONVERSION EFFICIENCY DATA ON LAST GROUP OF SUBMITTED CELLS

Cell Number	Incoming sunlight energy in mw cm^{-2}	I_{sc} in ma	I_{sc} at 100 mw in ma cm^{-2}	I_{sc} Tungsten in ma cm^{-2}	Sunlight conversion efficiency in percent
*C-2A	104.0	21.0 (IXI)	23.64	28.2	9.2
*C-2B	104.0	21.0 (IXI)	23.64	28.8	9.5
*C-2C	103.5	20.5 (IXI)	23.29	27.7	9.4
C-2D	104.0	20.0 (IXI)	22.58	27.6	8.7
C-2E	104.0	19.5 (IXI)	22.00	26.5	8.9
*C-3A	104.0	44.5	23.08	28.4	9.0
*C-3B	104.0	48.0	24.91	30.0	9.6

*Denotes cells submitted to GSFC for evaluation

prefix letter of C are the control cells, those with prefix letter-numbers E33 are the gas impurity cells, and those with letter-numbers E34 and E35 are the cells fabricated after the gas impurity situation was rectified. It is evident that the short circuit current density in sunlight illumination of the good cells is equal to or better than the control cells, while the current density of the seven gas impurity cells is equal to about 75 percent of the control cell current density.

Since the control cells yielded conversion efficiencies no greater than 9.6 percent, it was not expected that drift cells would yield efficiencies higher than this; the highest value observed being 9.3 percent, and the lowest 6.5 percent. Although it is not representative to analyze the results of only 37 cells on a statistical basis, a preliminary evaluation shows the mean cell to be 7.7 percent, the median cell as 7.6 percent and the modal cell about 7.4 percent. This would indicate a Gaussian distribution with a slight skew toward the lower value end. In calculating the efficiencies of 1 x 2 cm cells, the active area was taken to be 1.85 cm^2, while the active area of 1 x 1 cm cells was taken as 0.85 cm^2, since the contact strip and grid area is only 0.15 cm^2 on both types of cells. No allowance was made for edge chipping.

At the time the epitaxial cells were being fabricated, spectral response measuring equipment was in the process of being assembled. The apparatus consisted primarily of an Aminco single-pass double-slit monochrometer, and a tungsten, quartz envelope iodine atmosphere lamp operated at 3,400^{o}K. The data taken on the epitaxial cells were corrected for constant energy by use of a standard solar cell with a known spectral response. The results are shown in Fig. 12.

Since the curves are not normalized, it is obvious that a shift of the peak response into the blue portion of the spectrum is occurring. The most salient feature is the narrowness of the curves compared to the standard cell, the dropoff in the red being most probably due to loss of minority carrier lifetime deeper in the cell due

to the higher boron concentration. The dropoff in the blue is perhaps due to a deeper junction.

Measurements were also taken on a number of field-free control cells fabricated from material similar to the 25Ω-cm material used on the epitaxial drift cells.

Figure 13 shows the spectral response of four types of cells.

1. C-1A is a control cell as described above
2. E26-4A is one of the reverse epitaxial drift field cells
3. B-43A5 is an EOS diffused drift field cell with approximately 100μ drift field region
4. Is a standard n-on-p cell

The loss of red response of the epitaxial cell compared to the control cell is apparent. The characteristic of the diffused drift cell indicates collection from deeper within the cell, most probably due to the deeper aiding field compared to the shallower epitaxial cell.

To gain insight into the loss of red response on the drift field cells, it was decided to fabricate another group of control cells. These cells, labeled C-3, were fabricated by precisely the same procedure and from the same material as the control cells of C-1 series, except that the back contact boron tack-on diffusion was not performed. Comparing the spectral response characteristics (cell C-1A in Fig. 13 and cell C-3B in Fig. 14), it is entirely possible that the extra heat treatment required for the back contact boron tack-on diffusion is responsible for the loss of red response of cell C-1A over C-3B.

Drift field cells, of necessity, receive at least three (and sometimes four) heat treatments at temperatures greater than $1000^{\circ}C$. It is highly probable that these repeated heat treatments are the cause of loss of minority carrier lifetime which result in the poor red response.

A comparison can also be made between the spectral response of a sample cell fabricated with the strains resulting from the "gas impurity" condition and a sample of the latest epitaxial cells (see
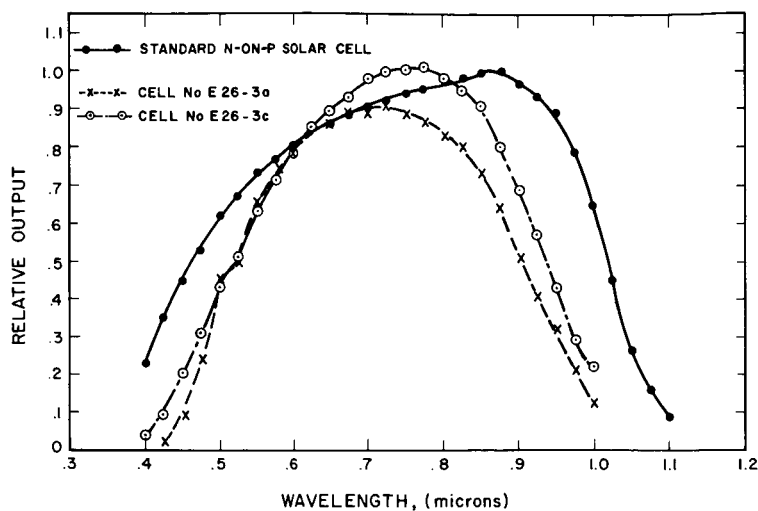
FIG. 12

SPECTRAL RESPONSE OF EPITAXIAL
DRIFT FIELD CELLS COMPARED TO
STANDARD N-ON-P CELL

FIG. 13

RESULTS OF SPECTRAL RESPONSE
MEASUREMENTS ON VARIOUS DRIFT
FIELD AND FIELD FREE SOLAR
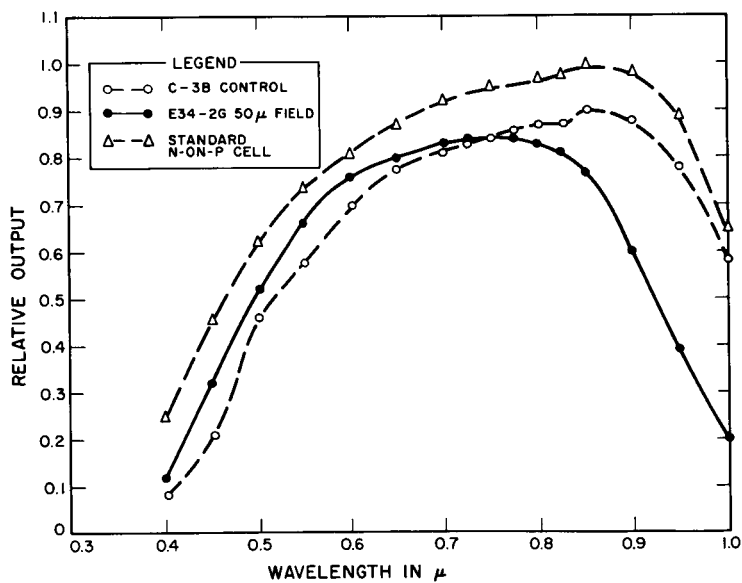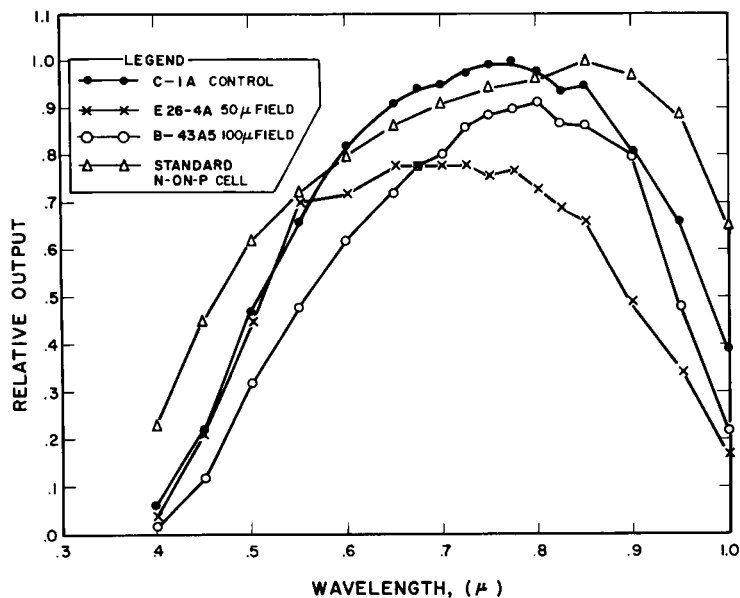CELLS

FIG. 14

SPECTRAL RESPONSES OF CONTROL,
STANDARD AND RECENT EPITAXIAL
DRIFT FIELD CELL

curve of cell E26-4A in Fig. 13, and cell E34-2G in Fig. 14). The "strained" cell has a low, flat response from 0.65 to 0.8 micron; whereas the "nonstrained" cell, although possessing much less red response than either a standard n-on-p or a control cell, has a definite broad peak at 0.75 micron.

5. RADIATION DAMAGE EXPERIMENTAL RESULTS

5.1 First Group of Radiation Data

Table VIII summarizes the results and offers a basis of comparing the various drift cells against two RCA standard n-on-p field-free cells. For each cell four items are listed for each condition (e.g., before irradiation and after each subsequent 1 Mev electron dose). The first item is the curve power factor given in percent, which can be expressed as

$$CPF = \frac{P_{max}}{I_{sc} \cdot V_{oc}} \qquad (25)$$

The CPF would indicate any degradation or change in the shape of each cell after each successive dose of radiation due to an increase in the "A" factor of the diode equation or an increase in the series resistance.

The second and third items of the table list the short circuit current I_{sc} and the open circuit voltage V_{oc} of each cell for each successive irradiation. The last item indicates the percentage of maximum power P_{max} retained by each cell after each irradiation compared to its initial P_{max}.

A comparison of the CPF of all cells indicates that no appreciable degradation of the shape of the I-V characteristic occurs. A plot of log $(I_{sc}-I)$ versus V of cell E26-la whose CPF has degraded from 73 to 69 shows the slope of the initial condition plot to be parallel to the I-V curve plot of the cell after 2×10^{16} total electrons (see Fig. 15). The slight CPF degradation is apparently due not to an increase of the diode equation "A" factor at the knee of the I-V characteristic curve, but perhaps to an increase of

TABLE VIII

SUMMARY OF RESULTS OF FIRST TWO IRRADIATIONS

Cell No.	Before Irradiation			After 5×10^{14} 1 Mev Electrons				After 5×10^{15} 1 Mev Electrons			
	CPF in %	V_{oc} in volts	I_{sc} in ma	CPF in %	V_{oc} in volts	I_{sc} in ma	% of P_{max} retained	CPF in %	V_{oc} in volts	I_{sc} in ma	% of P_{max} retained
A3-2	73	0.490	45.0	72	0.465	42.5	79.5	72	0.420	34.0	58.0
A2-8	67	0.480	44.0	66	0.465	40.5	76.5	64	0.430	34.0	57.0
A6-5	70	0.540	46.0	70	0.490	44.0	81.5	70	0.430	36.5	60.0
A9-1	48	0.420	35.0		0.405	31.0	84.0		0.370	22.0	57.0
A9-2	65	0.535	16.0	65	0.520	13.8	81.5	64	0.480	9.0	50.0
E26-1a	73	0.490	45.5	72	0.470	44.0	90.0	73	0.425	37.0	70.5
E26-1b	74	0.480	39.5	74	0.455	38.5	91.5	70	0.425	34.0	75.5
E26-2	72	0.520	38.0	73	0.485	37.0	91.5	73	0.430	31.0	70.0
E26-3a	71	0.560	35.5	71	0.540	31.0	85.5	70	0.485	23.5	57.0
E26-3c	68	0.552	35.0	70	0.532	31.5	88.0	67	0.470	26.0	62.5
E26-4b	72	0.532	40.5	74	0.512	37.0	90.0	71	0.457	32.5	70.5
RCA-1	65	0.550	129.0	66	0.485	99.0	71.0	65	0.440	77.0	49.5
RCA-7	66	0.540	127.0	67	0.485	97.0	69.0	66	0.440	76.0	49.0

TABLE VIII (contd)

SUMMARY OF RESULTS OF FIRST TWO IRRADIATIONS

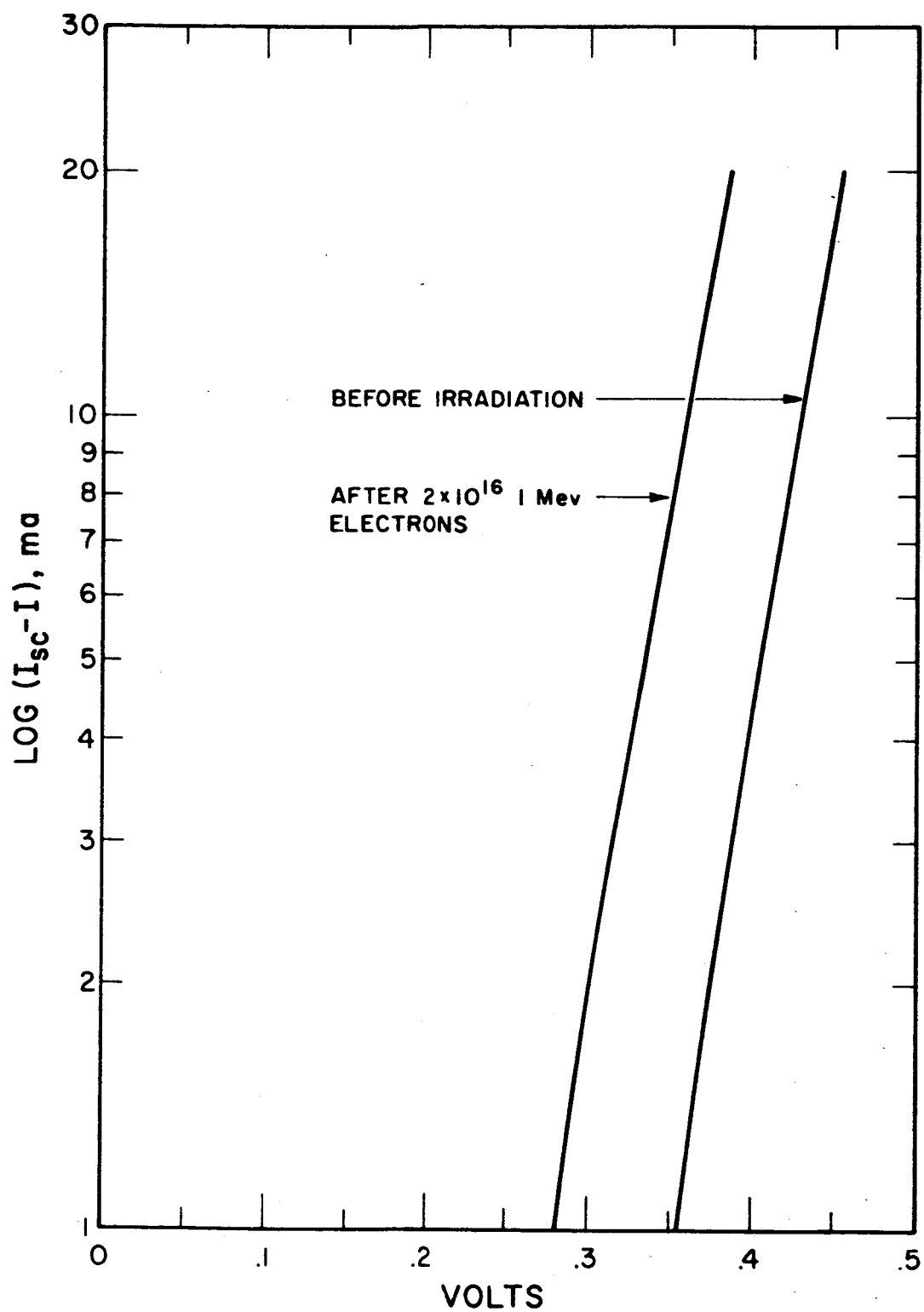| Cell No.	After 1 x 10^16 1 Mev Electrons				After 2 x 10^16 1 Mev Electrons			
	CPF in %	V_{oc} in volts	I_{sc} in ma	% of P_{max} retained	CPF in %	V_{oc} in volts	I_{sc} in ma	% of P_{max} retained
A3-2	70	0.415	32.0	53.5	69	0.395	31.5	49.0
A2-8	64	0.420	31.0	53.0	64	0.405	30.5	49.5
A6-5	69	0.420	34.0	54.5	68	0.405	33.0	49.0
A9-1		0.350	18.5	43.0		0.335	16.5	36.0
A9-2	63	0.405	7.6	40.0	61	0.440	6.7	33.0
E26-1a	69	0.415	35.0	62.0	69	0.410	34.0	58.5
E26-1b	70	0.42	31.5	67.0	70	0.405	31.0	63.0
E26-2	70	0.425	28.5	60.0	69	0.410	27.0	56.0
E26-3a	68	0.470	20.5	48.5	68	0.458	18.0	41.5
E26-3c	67	0.458	23.0	53.5	67	0.442	20.3	46.0
E26-4b	72	0.448	30.5	64.0	72	0.430	28.5	57.5
RCA-1	64	0.435	73.0	47.0	64	0.425	69.0	41.5
RCA-7	63	0.435	69.0	41.0	64	0.420	66.0	40.0

FIG. 15 PLOT OF LOG (I_{sc}-I) VERSUS V OF CELL E26-1a

the series resistance of the cell or an increase of the shunt current or saturation current, each of which would contribute to a degraded CPF. However, these increases are not evident from the supplied I-V curves due to the compressed scales, but would be so, if present, in an accurate point-by-point measurement.

The most significant point in the comparison of the aluminum alloy diffused cells (prefix A2 to A9) is the obvious complete degradation of the two cells of the A9 series (worse than the standard n-on-p in percent of P_{max} retained) compared to the A2, A3 and A6 cells (slightly better than the n-on-p in P_{max} retained). Cells A2-8, A3-2, and A6-5 were fabricated from material supplied by a manufacturer different from that which supplied the material for the A9 series.

In comparing the reverse epitaxial cells of the E26 series to both the aluminum alloy diffused cells and the RCA field free cells, it is evident that the epitaxial cells are superior in percent of P_{max} retention. After 5×10^{15} electrons, the best of the epitaxial cells have retained 70 percent of maximum power as opposed to only 50 percent retention by the field-free cells. Proportionately, after 2×10^{16} electrons the epitaxial cells retained on the average of 60 percent of their power compared to only 40 percent by the field-free cells.

Considering the absolute efficiencies, the best epitaxial cells have an average conversion efficiency of 4.5 percent after 2×10^{16} electrons, which is comparable to the RCA field-free cells; however, the initial efficiency of the drift cells was between 7 to 8 percent compared to approximately 11 percent for the field-free cells. Cell E26-1a still possesses an efficiency of 4.8 percent after 2×10^{16} electrons with an initial efficiency of 8.2 percent compared to 4.6 percent and 11.4 percent respectively of the best field-free cell.

5.2 Second Group of Radiation Data

Analysis of the second group of radiation damage data received was divided into three categories:

1. An analysis of short circuit current degradation.

2. A preliminary study of the diode equation "A" factor and consequent saturation current change with increased radiation flux and their combined effect on open circuit voltage degradation.

3. An analysis of the loss in total efficiency.

5.2.1 Short Circuit Current Degradation

As would be expected, an electrostatic field incorporated in the base region of a solar cell aids in the collection of minority carriers generated in this region. After extremely large doses of radiation, $> 10^{15}$ particles, the short circuit current in field-free solar cells degrades due to loss of minority carrier lifetime by an increased recombination rate. Collection of minority carriers in drift-field cells, on the other hand, is not totally dependent on lifetime, the field aiding in the carrier collection to some extent initially, and more so after a high percentage of the lifetime has been reduced by radiation.

This theory was substantiated strongly by the experimental results. Figure 16 shows the percent of short circuit current retained after successive irradiation on the arithmetically mean cell of the supplied data. The following is a list of cells of each manufacturer on which the mean was computed:

EOS Cells 34-2A, 34-2D, 34-3A, 34-3C, 34-3E, 35-1C, 35-2A, 35-2E, 35-2C, 35-3A, and 35-3D

Heliotek Cells 23, 24, 25, 31, 32, 33, 34, 35, and 36

Texas Inst. Cells 4, 21, 22, 24, 26, 28, 30, 35, 38, and 39

RCA ⟨100⟩ Cells 261, 273, 274, 270, 271, 272, 269, 267, 268, 279, and 280

RCA ⟨111⟩ and ⟨110⟩ Cells 201, 206, 208, 209, 212, and 216

Radiation damage data on the cells of the other manufacturers was provided concurrently with data from EOS cells by the contract monitor for a basis of comparison.
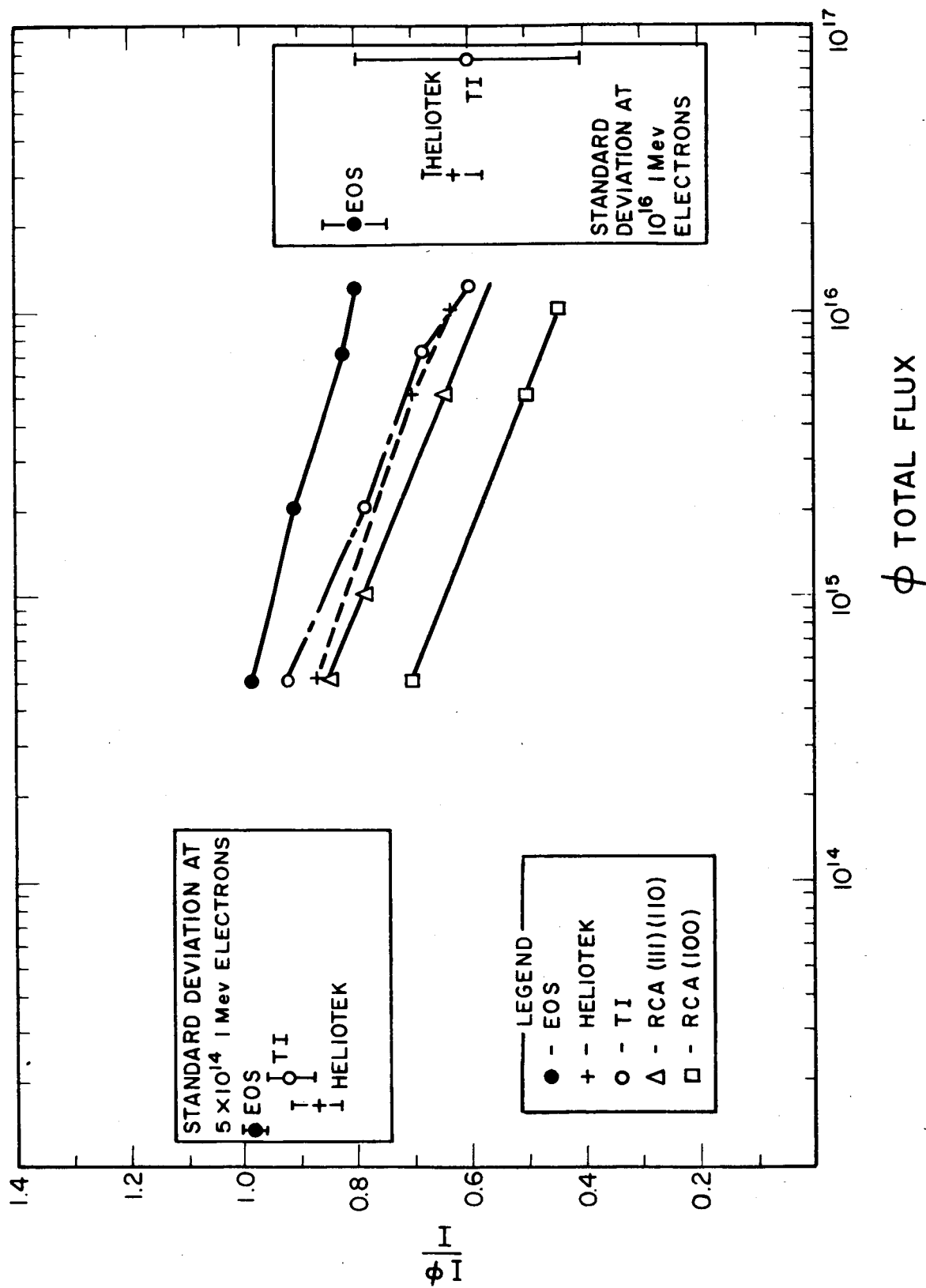
FIG. 16   MEAN CELL OF EACH MANUFACTURER PERCENT SHORT CIRCUIT CURRENT RETAINED

Electro-Optical Systems, Inc. Cells 33-1B, 33-2B, 33-3B, 34-1D, and 34-1E were not considered in the data grouping since these cells were fabricated under the epitaxial "nitrogen gas leak condition" explained above.

It should be noted in Fig. 16 that the EOS mean cell has retained 80 percent of the original short circuit current after 10^{16} 1 Mev electrons. In comparison, only 60 percent of the I_{sc} was retained by the Heliotek and TI drift cells and $\langle 111 \rangle$ and $\langle 110 \rangle$ RCA standard field-free cells, and only 42 percent by $\langle 100 \rangle$ RCA standard cells. The anisotropic behavior of the RCA cells cannot be explained at present.

The standard deviation, σ, was calculated as

$$\sigma = \sqrt{\frac{\Sigma(X^2)}{N}} \tag{26}$$

where X = deviation from arithmetic mean $(X - \bar{X})$

   N = total number of cells

the significance of σ being that 68 percent of the values lie within σ and 95 percent lie within 2σ. The fact that the value of σ for both the EOS and Heliotek cells is small at 10^{16} electrons tends to indicate that some measure of process control has been achieved. However, since the EOS mean cell is approximately 20 percent higher in I_{sc} retention at this radiation flux than the Heliotek mean cell, indications are that a more optimum field-depth ratio has been attained in the EOS cell. Because of the high value of σ for the TI cells, no conclusions can be made for these samples at present.

Another fact which indicates an optimum field-depth ratio in the EOS cells is the small degradation of the quantum yield as a function of total radiant flux at the longer wavelengths. Electro-Optical Systems cells 34-2A through 35-2E exhibit small percentages of degradation throughout the spectrum. Cells 35-2C, 35-3A, and 35-3D exhibit a higher percentage loss in the red portion of the spectrum due to the fact that the cells were lapped and etched more during

fabrication, thus placing the junction farther in the diffused field region and, consequently, into lower resistivity material. This correlates with the fact that these three cells possess initial open circuit voltages of 550 millivolts, as opposed to lower open circuit voltages for the former cells. The loss of red response in the latter cells would tend to indicate that a percentage of photon absorption, generation and collection, was evident in the field-free region beyond the drift field prior to irradiation (see Figs. 17 and 18).

Further evidence of this fact is given upon consideration of Heliotek drift-field cells numbers 23 through 36, which exhibited an initial high response beyond the 0.8μ region with subsequent loss of this response after irradiation. As stated in Heliotek progress reports (Ref. 16), the drift field thickness in these cells was on the order of 30 microns or less, and the loss of red response would indicate absorption and initial collection from beyond the field region. TI has shown that approximately 30 percent of 0.9μ wavelength photons are absorbed at distances greater than 30 microns below the surface in silicon, this percentage increasing with longer wavelengths (Ref. 12). Both the Heliotek drift field cells and the three mentioned EOS cells tend to indicate this to be true and, therefore, it seems empirically probable from this evidence that an optimum drift field thickness is at least 50 microns.

5.2.2 Open Circuit Voltage Degradation

Evidence in Fig. 19, which plots percent of open circuit voltage retained versus total radiation flux, indicates that the $\langle 111 \rangle$, $\langle 110 \rangle$ RCA field-free cells show a shallower slope in V_{oc} degradation than any of the drift-field cells, the $\langle 100 \rangle$ RCA cells having a slope approximately equal to that of the drift cells. Contrasting this information with Fig. 16 would lead one to believe that the open circuit voltage is strongly dependent on factors other than the light generated current.
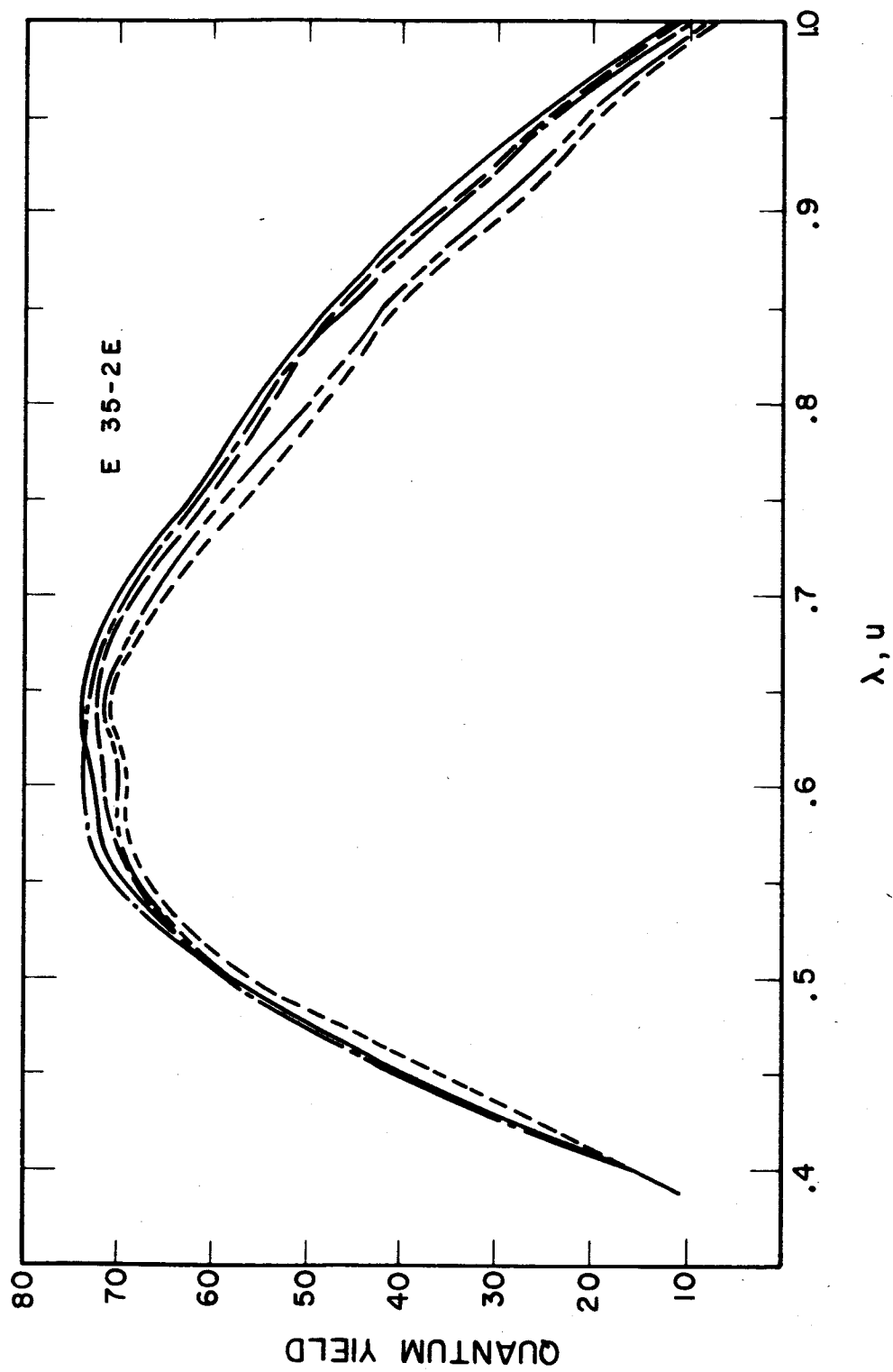
FIG. 17 QUANTUM YIELD VERSUS WAVELENGTH RESPONSE BEFORE AND AFTER SUCCESSIVE IRRADIATIONS
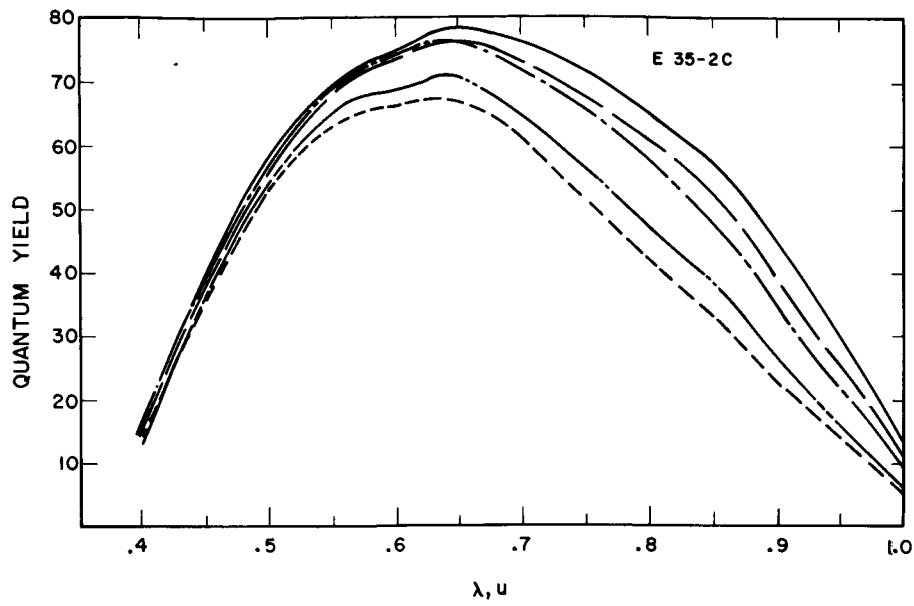
FIG. 18   QUANTUM YIELD VERSUS WAVELENGTH RESPONSE BEFORE
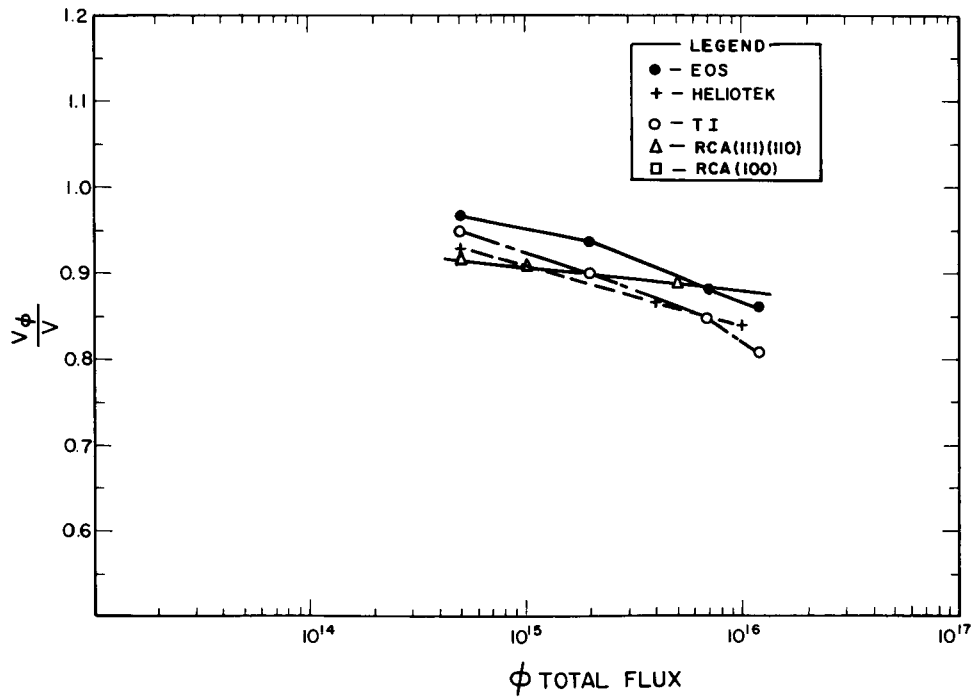   AND AFTER SUCCESSIVE IRRADIATIONS

FIG. 19   MEAN CELL OF EACH MANUFACTURER PERCENT OPEN
          CIRCUIT VOLTAGE RETAINED

In Figs. 20 and 21, the log $|I-I_{sc}|$ versus voltage plots are considered, both before and after irradiation of EOS cell E34-2A, which has a V_{oc} retention of 89 percent, and cell E35-2C, which retains only 82 percent of its open circuit voltage. Considering cell E34-2A, the slopes of the log $|I-I_{sc}|$ versus voltage plot apparently do not change before and after irradiation. Using the empirical value of 10^{-7} amperes for I_o in Fig. 3 before irradiation and solving for A in Eq. 16, a value of 1.37 is obtained. After irradiation, cell E34-2A has an I_o value of 4×10^{-7} and a resulting A factor of 1.38.

Solving for A with values of I_o of 5×10^{-7} and 1.5×10^{-5} obtained from Fig. 21 before and after irradiation, respectively, for cell E35-2C, values of A of 1.8 and 2.2 are obtained. These examples are chosen as representative of the two distinct groups of EOS cells mentioned in Subsection 5.2.1, e.g., those with an initially low V_{oc} and greater retention, and those with an initially higher open circuit voltage and less retention.

Similar plots of log $|I-I_{sc}|$ of the RCA cells show a decrease of A factor and consequent decrease of I_o after irradiation (Figs. 22 and 23). This anomalous result cannot be explained at present, except perhaps by the fact that the data was taken from the compressed curves supplied by GSFC.

Results of calculations of τ from Eq. 20 for cells E34-2A and E35-2C using values of w taken from graphs given by Ref. 13 under zero bias conditions and assuming the junction potential at 0.7 volt are shown in Table IX. The value of base impurity concentration was taken to be 5×10^{14} atoms cm^{-3} for cell E34-2A and 10^{16} atoms cm^{-3} for cell E35-2C. The values obtained for τ in the immediate vicinity of the junction are reasonable and in fair agreement with published data (Refs. 14 and 15).
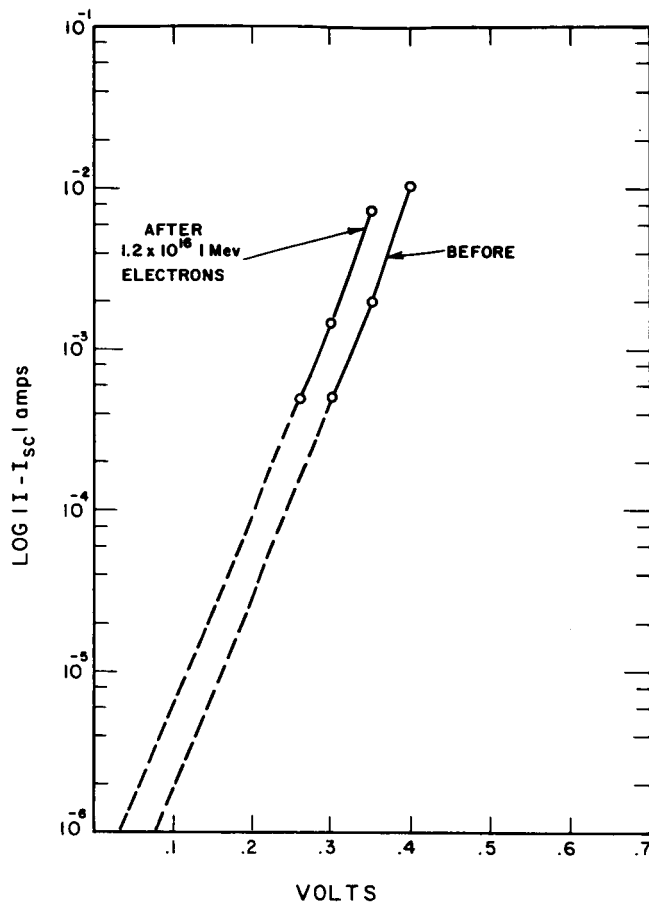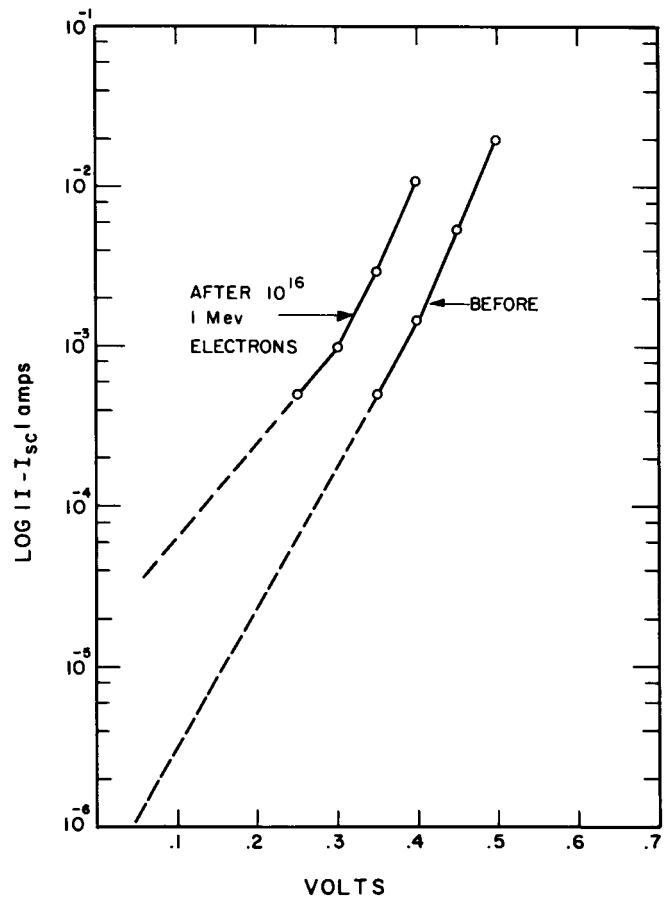
FIG. 20
EOS CELL NO. E34-2A
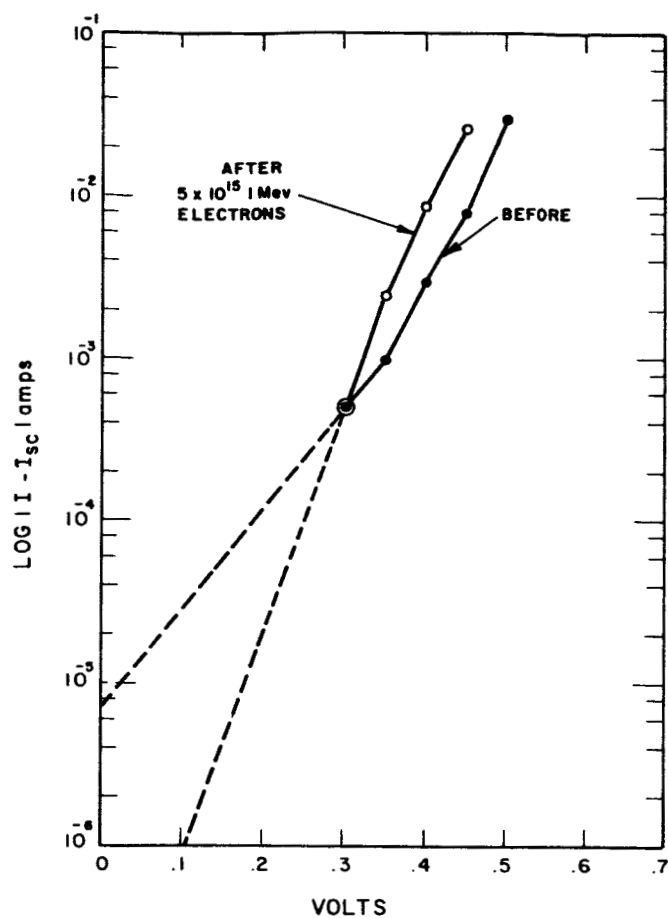

FIG. 21
EOS CELL NO. E35-2C

FIG. 22
RCA CELL NO. 208 (110)

FIG. 23
RCA CELL NO. 270 (100)
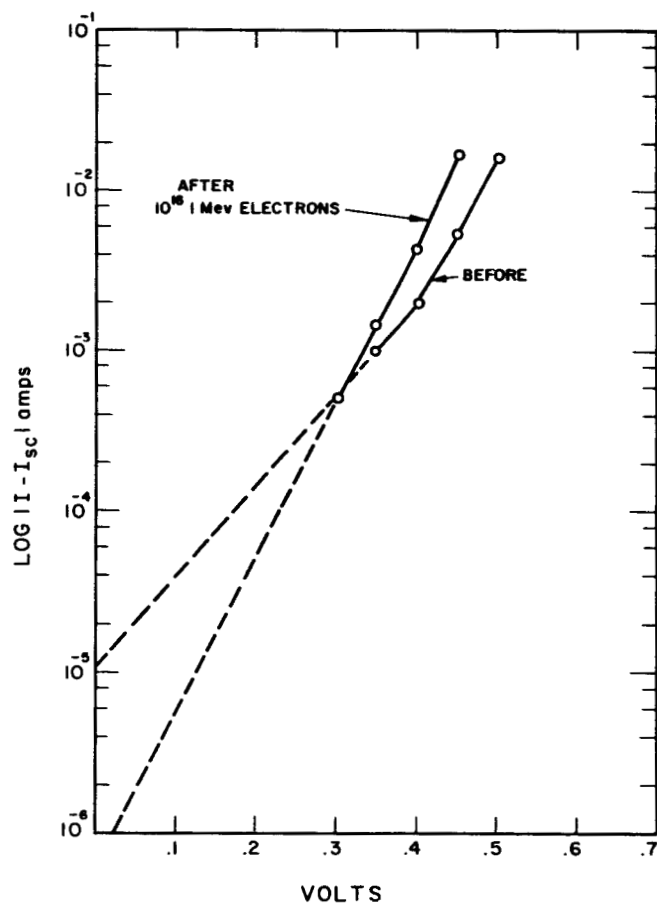
TABLE IX

CALCULATIONS OF MINORITY CARRIER LIFETIME τ

BEFORE AND AFTER IRRADIATION

Cell Number		I_o	ℓ	τ
E34-2A	before	10^{-7} amps		3×10^{-6} secs
	after 1.2 x 10^{16} electrons	4×10^{-7} amps	1.5×10^{-4} cm	8×10^{-7} secs
E35-2C	before	5×10^{-7} amps		2×10^{-7} secs
	after 1.2 x 10^{16} electrons	1.5×10^{-5} amps	5×10^{-5} cm	3×10^{-9} secs

Electro-Optical Systems cells E34-2A through E35-2E, which exhibit a relatively small decrease in I_{sc}, V_{oc}, and consequent efficiency and show little or no increase in A factor, obviously possess an effective drift field. Since in these cells the collection of generated carriers is not heavily dependent on minority carrier life-time τ, we must consider an effective τ which shows little change after irradiation with no consequent change in A factor nor I_o. Opposed to this are the three nonoptimum cells which exhibit a loss of red response, a greater loss in efficiency, and a loss of true minority carrier life-time τ, on which their generated carrier collection is dependent, as evidenced by the increase in I_o and A factor and consequent greater degradation of V_{oc} after irradiation.

This calculation is of great importance and indicates that the open circuit voltage degradation is predictable and under-standable for some selected cells.

In the calculation, it was assumed that I_o (the junction leakage current) is due to generation in the junction space charge region. I_o was estimated before and after irradiation by replotting the Goddard I-V characteristics on a semilog plot.

The values of τ found from this calculation agree well with what is to be expected from previous published data. For example, cell E34-2A had a lifetime of 3×10^{-6} seconds before irradiation, and 8×10^{-7} seconds after 1.2×10^{16} electron flux as computed from the I-V characteristics. These values correspond to electron diffusion lengths of 110μ and 55μ respectively and show reasonable agreement with previous data for L_p under these conditions (Refs. 14 and 15).

5.2.3 Total Efficiency Degradation

Figure 24 shows the degradation of absolute efficiency with increased flux of the mean cell of each manufacturer. The arith-metic mean was calculated on the same samples mentioned above. It is apparent from the shallower slope of the EOS cells that a more optimum
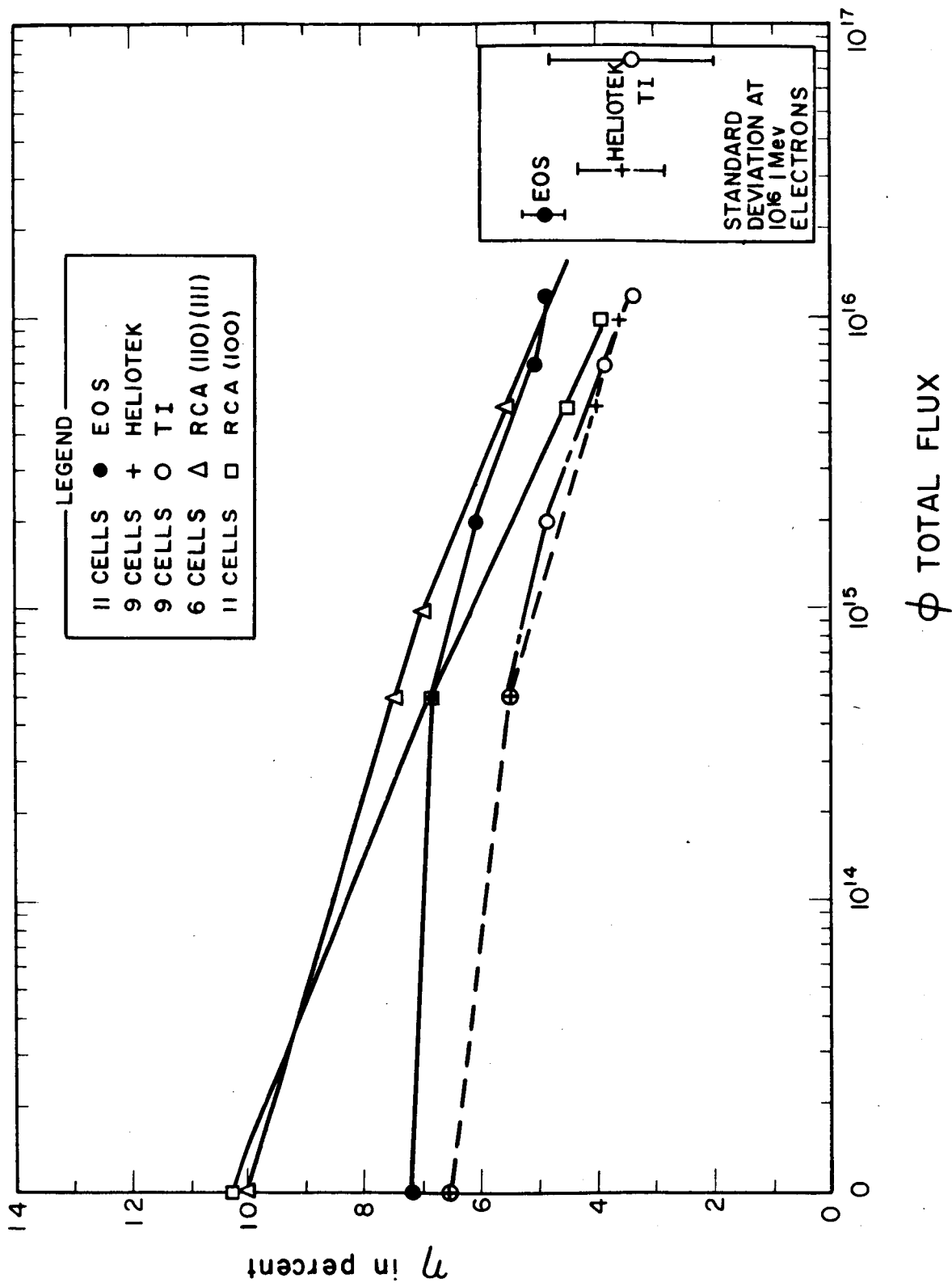
FIG. 24 MEAN CELL OF EACH MANUFACTURER ABSOLUTE EFFICIENCY

field-depth ratio exists, with the small value of σ again denoting greater process control. The larger value of σ for the Heliotek cells stems from the larger fluctuation of V_{oc} retention. This extremely wide variation in the TI cells is commensurate with the large value of σ in I_{sc} retention. A point to note is the more shallow slope of the EOS cells at the 10^{16} electron flux level, and it would be interesting to see how these cells would behave at still larger flux levels, so that, even though standard cells (such as the RCA samples) have higher initial values of conversion efficiency, the optimized drift field cells should remain more efficient after 10^{17} and 10^{18} particles.

6.   COMPARISON OF EXPERIMENTAL RESULTS TO THEORETICAL CALCULATIONS

The experimental results of irradiations performed at GSFC indicate
that an optimum field thickness exists in the vicinity of at least 50
microns. Cells with field regions < 50 microns exhibit relatively
more degradation with increased radiation flux due to absorption of
photons and generation of carriers beyond the field region. Since
the subsequent collection of these carriers, generated outside the
field region, is lifetime dependent, the collection efficiency drops
due to absence of an aiding field. Those cells possessing field
thicknesses of 50 microns exhibited less degradation of short circuit
current due to the absorption of the majority of photons and genera-
tion of carriers within the aiding field.

This experimental data agrees well with the computer calculated
data in the fact that a field thickness minimum of approximately 50
microns is indicated in both instances. Since the forcing integral
was assumed to be negligible beyond the field region in the solution
of the equation, a simile exists between the calculated data and ex-
perimental results. In the cells with thin field regions, the collec-
tion efficiency in the field free region quickly degraded upon irradia-
tion, so that in essence the generation and collection of carriers in
this region was negligible, the only contribution to short-circuit
current coming from the thin field aided region toward the front of
the cell.

In view of the qualitative agreement between the theoretical and
experimental data on the degradation of short-circuit current, the
principal problem remaining is the understanding of the degradation of
open circuit voltage. The insight gained by the calculations of τ
from Jonscher's expression for saturation current generation in the
space charge region from Eq. 20 is significant.

The computer solution indicates the optimum field thickness of a cell having a residual lifetime of approximately 10^{-6} seconds to be somewhere between 50 and 100 microns and an experimental substantiation is thus obtained. A cell which proved to be near optimum experimentally indeed possessed a residual lifetime of nearly 8×10^{-7} seconds, as predicted by the calculated equation. This becomes important considering the dependence of open-circuit voltage retention on changes in I_o and A factor both of which are, in turn, dependent on minority carrier lifetime. In view of these results, it is felt at this time that significant future insight can be gained by accurate measurements of solar cell characteristics before and after irradiation to determine I_o, A factor and lifetime, both calculated and measured. This data in conjunction with future modifications and extensions to the solution of the continuity equation could be used to predict optimum field widths tailored to specific space mission requirements.

7. RECOMMENDATIONS FOR FUTURE WORK

In view of the significant agreement between the theoretical calculations and the experimental results for short-circuit current degradation presented above, future work should include more positive verification of these results, especially the resolution of the optimum field depth question. A further research and development effort is indicated to provide information and insight into the open circuit voltage degradation problem.

It is recommended that longer range plans include an unbalanced pilot line program to acquire realistic process yield figures and manufacturing costs and to provide statistical data as a basis of projection of the performance of drift field cells in typical near-earth orbits. Experience gained from the pilot line would also present a basis of preparation of complete process specifications for the manufacture of the cells.

REFERENCES

1. D. A. Kleinman, "Considerations of the Solar Cell," *Bell Systems Tech. Journal*, Vol. 40, No. 85, 1961

2. M. Cheslow and S. Kaye, "Feasibility Study Toward Development of a Radiation Resistant Solar Cell," Electro-Optical Systems, Inc., Final Report, Contract No. NAS7-92, Feb 1963

3. M. Wolf, "Drift Fields in Photovoltaic Solar Energy Converter Cells," *Proc. of IEEE*, Vol. 51, No. 5, May 1963, p. 674

4. K. B. Wolfstirn, "Hole and Electron Mobilities in Doped Silicon from Radiochemical and Conductivity Measurements," *J. Phys. Chem. Solids*, Vol. 16, 1960, pp. 279-284

5. A. K. Jonscher, "Principles of Semiconductor Device Operation," John Wiley & Sons, Inc., 1960

6. V. Sils and P. Wang, "A Technique for The Determination of Impurity Concentration Gradients in Silicon Epitaxial Layers," paper presented at the spring meeting of The Electrochemical Society, Los Angeles, California, May 1962

7. Thomas, Kahng and Manz, "Impurity Distribution in Epitaxial Silicon Films," *J. Electrochem. Soc.*, Nov 1962, p. 1055

8. J. C. Irvin, "Resistivity of Bulk Silicon and of Diffused Layers in Silicon," Bell Telephone Systems Monograph No. 4092

9. T. B. Light, "Imperfections in Germanium and Silicon Epitaxial Films," paper presented at Conference on the Metallurgy of Semiconductor Materials, Ambassador Hotel, Los Angeles, California, 1961 (proc. published by John Wiley & Sons)

10. E. F. Cove and B. R. Czarny, "Epitaxial Deposition of Silicon and Germanium Layers by Chloride Reduction," *RCA Review*, Vol. 24, No. 4, Dec 1963, p. 523

11. S. E. Mayer and D. E. Shea, "Epitaxial Deposition of Silicon Layers by Pyrolysis of Silane," *J. Electrochem. Soc.*, May 1964, p. 550

REFERENCES (contd.)

12. First Periodic Progress Reports, "Development of Epitaxial Struc-
    tures for Radiation Resistant Silicon Solar Cells," performed by
    Texas Instruments, covering period 1 Oct 1963 to 31 Mar 1964,
    NASA Contract NAS5-3559, p. 22

13. H. Lawrence and R. M. Warner, Jr., "Diffused Junction Depletion
    Layer Calculations," Bell Telephone Laboratories Monograph No.
    3517

14. J. M. Denney and Downing, "Summary of Radiation Damage Studies
    at STL," paper presented at the Proceedings of the Solar Working
    Group Conference, Feb 1962

15. "Radiation Damage to Silicon," Final Report, work performed by
    RCA, David Sarnoff Research Center for NASA, Contract No. NAS5-457.

16. First and Second Periodic Progress Reports, "Development of an
    Improved Radiation Resistant Solar Cell," performed by Heliotek,
    Inc., NASA Contract NAS5-3558, 8 May 1964 and 10 Nov 1964